Nuclear Physics B150 (1979) 221–267

MEASUREMENTS OF ELASTIC PROTON-PROTON SCATTERING AT LARGE MOMENTUM TRANSFER AT THE CERN INTERSECTING STORAGE RINGS

E. NAGY [1], R.S. ORR, W. SCHMIDT-PARZEFALL [2] and K. WINTER
CERN, Geneva, Switzerland

A. BRANDT [3], F.W. BÜSSER, G. FLÜGGE [2], F. NIEBERGALL and P.E. SCHUMACHER [4]
II. Institut für Experimentalphysik, Universität Hamburg, Germany ★

H. EICHINGER [5] and K.R. SCHUBERT
Institut für Hochenergiephysik, Universität Heidelberg, Germany

J.J. AUBERT, C. BROLL, G. COIGNET, H. DE KERRET, J. FAVIER, L. MASSONNET and M. VIVARGENT
Laboratoire d'Annecy de Physique des Particules, Annecy, France

W. BARTL, H. DIBON, Ch. GOTTFRIED, G. NEUHOFER and M. REGLER
Institut für Hochenergiephysik der Österreichischen Akademie der Wissenschaften, Wien, Austria ★★

Received 29 September 1978

Final results of our measurements of elastic proton-proton scattering at the CERN Intersecting Storage Rings (ISR) for c.m. energies $\sqrt{s}$ from 23 to 63 GeV and momentum transfers $|t|$ from 0.8 to 10 GeV^2 are presented. Absolute differential cross sections have been obtained using the split-field magnet detector facility (SFM) at the five standard energies for integrated luminosities ranging from 0.3 to 4.9 (pb)$^{-1}$. The rising total cross section is found to define a scale for diffractive phenomena near the forward peak, including the position of the diffraction minimum near $t = -1.4$ GeV^2. The cross section at the minimum is strongly energy dependent, approximately as the ratio of the

[1] Visitor from the Central Research Institute of Physics, Budapest, Hungary.
[2] Now at DESY, Hamburg, Germany.
[3] Now at Carl Zeiss, Oberkochen, Germany.
[4] Now at Lycée Gaston Diederich, Luxembourg, Luxembourg.
[5] Now at Institut für Hochenergiephysik, Wien, Austria.
★ Partially supported by Bundesministerium für Forschung und Technologie, Bonn.
★★ Partially supported by Fonds zur Förderung der wissenschaftlichen Forschung, Austria.

real to imaginary part of the scattering amplitude in the forward direction. The phase of the scattering amplitude is found to change sign near the minimum. The component of diffraction scattering beyond the second maximum has a much weaker t-dependence than expected in simple eikonal or constituent pictures connecting this region to the forward peak. A further break in slope is observed near $t = -6$ GeV^2. There is no evidence for another minimum for t values up to 10 GeV^2.

1. Introduction

The processes of diffraction scattering of hadrons reflect some fundamental properties of these particles; elastic diffraction scattering reflects the wave nature of the colliding hadron beams and the finite range of their strong interaction; inelastic diffraction is a direct manifestation of the internal structure of hadrons.

Among the numerous diffractive reactions, the elastic scattering of protons on protons provides the most favourable possibility for studying the diffraction mechanism at very high energy, as this channel does not display direct resonances, and non-diffractive contributions due to f^0, ω, ρ, and A_2 exchange are decreasing with increasing energy. There is a wealth of precise data at all proton accelerator energies. A study of the elastic scattering of protons on protons was therefore part of the first experimental program at the CERN intersecting storage rings (ISR) with the possibility of investigating diffraction scattering up to equivalent laboratory energies of 2000 GeV. At the time of the construction of this facility, an ever-shrinking differential cross section was expected when extrapolating results obtained at the CERN 28 GeV proton synchrotron (PS), with differential cross sections as low as 10^{-33} cm^2/GeV^2 at a value of four-momentum squared of $t = -1.5$ GeV^2.

The first experimental programme [1] at the ISR then led to the discovery of a diffraction-like minimum [2] near $t = -1.4$ GeV^2 and to new questions concerning the energy dependence of its position, of its depth and, of course, of the large-t behaviour of elastic scattering which now became accessible for experimental study.

On the other hand, the discovery of a rise of the total interaction cross section [3] over the ISR energy range by approximately 10% has led to new interest in the question of a simple geometrical scaling behaviour of elastic scattering at high energies [4,5].

We have therefore designed an experiment with the aim of measuring absolute values of the differential cross section, and in particular its energy dependence in the region of the diffraction minimum and beyond it.

The laboratory system at the ISR essentially coincides with the centre-of-mass system because of the small crossing angle ($\theta = 15°$) of the colliding beams. The scattered protons can therefore both be detected in a symmetric set-up, even at low four-momentum transfer. To make full use of this advantage of experimentation at the storage rings, we have chosen to use a large

solid-angle detector with magnetic field, the Split-Field Magnet facility (SFM), accepting t values up to 20 GeV^2.

Momentum analysis of both scattered protons is required to discriminate against the background of nearly elastic events, in particular at large-t values, as the increasing luminosity of the ISR allowed us to measure the differential cross section through ten orders of magnitude. Measurements of the directions and momenta of both scattered protons with experimental resolutions of $\Delta\theta = \pm 0.5$ mrad and $\Delta p/p = \pm 5\%$ gave adequate kinematical constraints and resulted in a residual background contamination of 2% to 5% for the full t-range covered.

Another advantage of experimentation at the ISR, in particular in searching for narrow minima and in measuring their depth, is the high resolution in four-momentum transfer t which can readily be achieved. In this experiment $\Delta t/t$ was typically 0.015, varying slowly and smoothly with t and with $\sqrt{s}$.

During this experiment we took data on elastic pp scattering in two periods, first from March to December 1974, together with data of the reaction $pp \to p\pi^+ n$ in its diffractive [6] and charge-exchange [7] * regions, and then from March to July 1976. Double-pomeron exchange candidates in the reaction $pp \to p\pi^+\pi^- p$ were taken in a small fraction of both periods [8]. The main results of the elastic scattering experiment have been published in several letters: the energy dependence of the dip position [9,10] in 1974/75, the non-existence of a second dip up to $|t| = 6.5$ GeV^2 in 1976 [11], and evidence for a third slope in the t region from 6.5 to 10 GeV in 1977 [12].

The t range of the results presented extends from 0.8 to 6 GeV^2 for all energies except $\sqrt{s} = 53$ GeV, where it extends from 0.8 to 10 GeV^2 owing to the higher ISR luminosity at this energy. The results obtained in 1975 for the t region below 0.8 GeV^2 have not been improved and are final already in ref. [10].

It is the purpose of this paper to describe the details of the set-up, the data analysis, the acceptance evaluation, and the final results of the experiment. The last sections are devoted to a confrontation of the results with recent theoretical attempts to describe elastic scattering.

2. The experimental set-up

2.1. The intersecting storage rings

The storage rings [13] are interlaced alternating gradient synchrotrons, intersecting each other in eight points. They are filled with protons which are accel-

* Ref. [7b] contains 1976 data.

erated in the CERN PS and then ejected from it. The highest energy of 31 GeV per beam is achieved by accelerating a beam of 26 GeV protons inside the ISR. The total energy in collisions of protons is

$$\sqrt{s} = 2E\sqrt{1 - \cos\tfrac{1}{2}\alpha}\,,$$

where E is the energy of the protons in each ring. The beams cross each other at an angle of $\alpha = 15^\circ$ in the horizontal plane. The ranges of energies available and of the equivalent energy of a proton hitting a stationary target are given in table 1.

The rate of beam-beam collisions is determined by the total cross section σ_{tot} and by the luminosity L:

$$\dot{N}_{\mathrm{tot}} = L \cdot \sigma_{\mathrm{tot}}\,.$$

The luminosity depends on the beam currents I_1 and I_2 (in amperes) and on the effective overlap height h_{eff} (in centimetres) of the crossing beams, according to

$$L = 10^{28}\frac{I_1 I_2}{h_{\mathrm{eff}}}\ (\mathrm{cm}^{-2}\ \mathrm{s}^{-1})\,. \tag{2.1}$$

Since the first operation in 1971, beam currents have increased steadily, up to 25–30 A at present; the effective beam height depends on the energy and is typically 0.3 cm. Typical luminosities available for data taking in 1974 and in 1976 are shown in table 1.

The lifetime of the coasting beams depends on the residual gas pressure in the beam tube and on the growth of the beam size due to multiple scattering. Average operating pressures as low as 10^{-10} Torr have been achieved, leading to half-lives of luminosity of about 30 hours, a figure which has been chosen as the typical length of a physics run before refilling.

Interactions of a beam with the residual gas in the crossing regions is a potential source of background in the experiments. With gas pressures of 10^{-11} Torr in the intersecting regions, the counting rate due to this background was typically between 1% and 20% of the beam-beam interaction rate. During high-luminosity runs, this ratio could only be kept within these limits by regular shaving of the beams.

2.2. The split-field magnet detector facility

A schematic view of the detector [14] is shown in fig. 1. It was installed in 1973 as a multipurpose and multiuser facility at the CERN ISR. The main magnet has a field volume of $10 \times 3 \times 1.10$ m^3 and was operated with fields of 0.50, 0.65, and 1.00 tesla at $\sqrt{s} = 23$, 31, and 45 GeV, respectively, and with 1.00 T also at 53 and 62 GeV. The two downstream magnets have a field volume of $2.50 \times 1.60 \times 0.40$ m^3 each, and were operated at nearly the same field values as the main magnet. They are compensating the deflection of the beams in the main magnet. The vacuum chamber has been enlarged near the intersection, as shown in fig. 2, to contain the deflected proton beams. It is fabricated using corrugated stainless steel, allowing a

Table 1
Summary of data acquisition

$\sqrt{s}$ (GeV)	23.46			30.54			44.64			52.81			62.07			All		
p_{lab}(eq.) (GeV)	292.4			496.2			1061.3			1485.7			2052.7					
Experiment	1974	1976	Total	1974	1976	Total	1974	1976	Total	1974	1976	Total	1974	1976	Total	1974	1976	Total
Luminosity (10^{30} cm^{-2} s^{-1})	0.1	1		0.1	1		1	2		2	4		0.5	1				
Integrated luminosity (pb^{-1})	0.03	0.37	0.40	0.02	0.43	0.45	0.16	0.27	0.43	1.09	3.84	4.93	0.03	0.26	0.29	1.33	5.17	6.50
Magnetic tapes	190	164	354	141	91	232	179	21	200	424	277	701	120	51	171	1054	604	1658
Triggers ($\times 10^6$)	6.3	7.2	13.5	3.5	2.1	5.6	2.5	0.6	3.1	10.6	4.8	15.4	3.3	1.4	4.7	26.2	16.1	42.3
Events after cuts ($\times 10^3$)	28	86	144	20	75	95	26	7.4	33	28	21	49	1.5	16	18	104	205	309

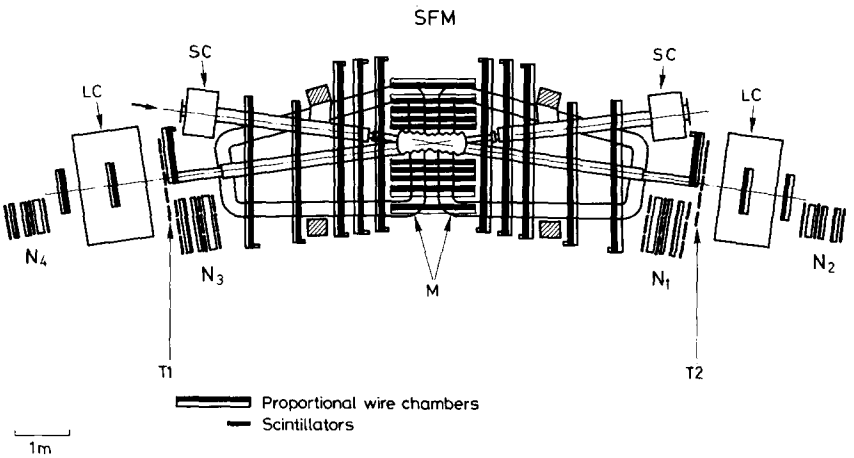

Fig. 1. The split field magnet (SFM) detector. M = main magnet; SC = small compensator magnet; LC = large compensator magnet; N_1, ..., N_4 = neutron vertex detectors; T_1 and T_2 = monitor scintillators.

wall thickness of 0.7 mm in the downstream arms. Absorption and multiple scattering of protons traversing the walls at small angles introduce large uncertainties in the differential cross sections at small t; a discussion of this limitation is given in subsect. 3.4.

The main magnet and the two compensator magnets are equipped with multiwire proportional chambers (MWPC) containing a total of about 70 000 wires and

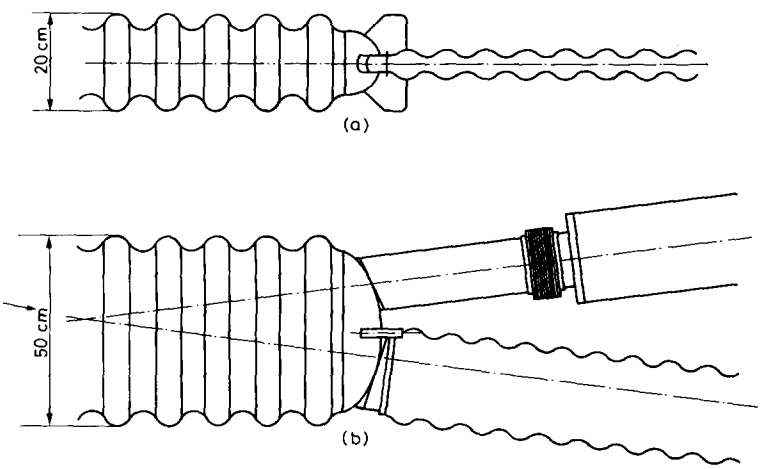

Fig. 2. (a) Side view and (b) top view of the vacuum chamber at the intersection.

one electronic channel per wire. Fourteen chambers [14] in each forward telescope cover a range of polar angles from 7 mrad to ~300 mrad. They consist of two orthogonal wire planes with 2 mm wire spacing. The high-voltage planes are divided into 5.6 cm wide strips from which a third and a fourth ($\pm 30^\circ$) coordinate are obtained to resolve multitrack ambiguities. The four central telescopes [15] consist each of one densely packed chamber with ten planes of wires in three directions and with 4 mm wire spacing. The horizontal central telescopes contain, in addition, two chambers with three planes, each with 4 mm wire spacing. Typical chamber areas are 2×1 m^2. The high voltage and the time window are chosen to obtain an efficiency larger than 0.995 for each wire plane. The thickness of a forward chamber is 0.010 collision lengths and 0.017 radiation lengths.

2.3. The trigger electronics

Large-t elastic scattering events have a cross-section of $\approx 10^{-3}$ mb for $|t| > 0.8$ GeV^2, i.e., $\approx 3 \times 10^{-5}$ of σ_{tot}. In order to reject other events as much as possible, a two-step decision logic was developed and was set up for large-t elastic scattering. As shown in fig. 3, fast signals from each wire and d.c. levels from each wire memory are used as logic inputs. In practice, only the OR functions of fast pulses from 256 adjacent wires (FOR) and the OR functions of 32 adjacent memory levels (MOR) have been used.

The fast decision logic [16] has been built using modular electronics (NIM) and has served to select events due to beam-beam interactions, suppressing events due to beam-gas interactions to a large extent, with a minimum requirement on topology for large-t elastic scattering events. The OR function of all horizontal wires in two adjacent forward chambers in coincidence with the OR of all their vertical wires

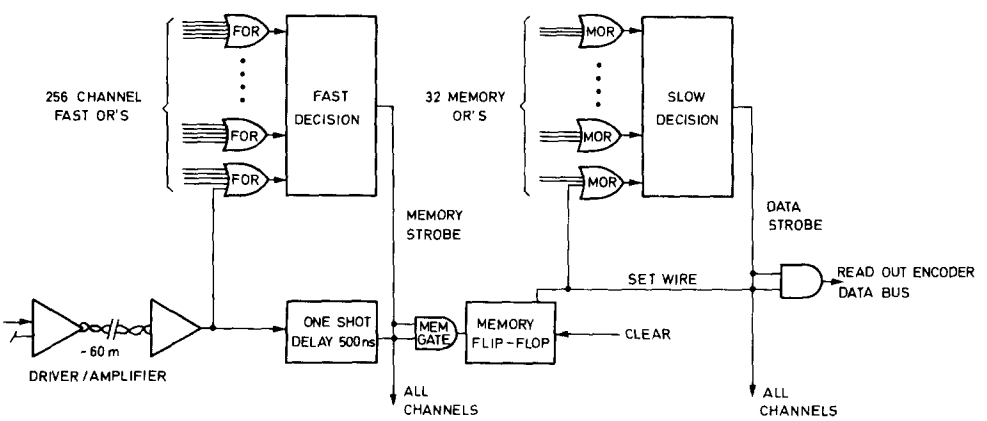

Fig. 3. Schematic diagram of the trigger electronics, showing how the fast and the slow decision are generated.

defined a hit in a chamber pair. The fast decision required at least three (for part of the time four) chamber pair hits in each one of the two forward telescopes, in anti-coincidence with a signal from the central telescopes to exclude events with additional tracks. To limit the t region of elastic scattering triggers, a hit of at least one vertical wire in a reference region of each forward telescope was required in addition. This region was chosen according to the ISR energy. A busy signal, which takes into account all dead-time contributions to the data acquisition (wire electronics, fast and slow decision, computer), was put in anticoincidence with the fast decision. An identical busy gate was applied to the signals of the scintillation counter monitors (subsect. 2.5). If the fast decision was positive, all wire memory gates were opened with a gate length of 150 ns (for part of the time 120 and 180 ns) and a subsequent slow decision was initiated.

The slow decision logic [17] was specially designed in TTL electronics using the memory OR levels mentioned above. Fig. 4 shows a sketch of the main tasks of this logic. In each one of the two forward telescopes the following functions F1 to F6 were available:

F1: number of hits per chamber pair (1 hit = 1 horizontal and 1 vertical group of 32 wires hit);

F2: one particle per telescope ($\geqslant$3 or 4 out of the first 6 chamber pairs with at least 1 hit);

F3: two particles per telescope ($\geqslant$3 chamber pairs with at least 2 hits);

F4: track finding in the vertical plane (see ref. [17] for details);

F5: combining θ_{vert}, the angle of the track found in F4, with θ_{horiz}, determined from a wire group in a reference plane, for a rough determination of the polar angle θ;

F6: collinearity, the functions F4 of both telescopes are combined to check if two tracks are roughly collinear in the vertical projection.

A large-t elastic scattering event was defined by a coincidence of the following functions: F2 (telescope 1) * F2 (telescope 2) * $\overline{\text{F3}}$ (telescope 1) * $\overline{\text{F3}}$ (telescope 2) * F4 (telescope 1) * F4 (telescope 2) * F6. For part of the data-taking time, it was also required that the angle θ determined by the function F5 corresponds to $|t| \gtrsim 0.8\ \text{GeV}^2$. This condition was later replaced by the reference plane condition in the fast decision. Information from the central telescopes was available in the fast decision only. For part of the time, also small-t elastic scattering was measured. The rough polar angle θ determined by F5 was then used to scale down the event rate by factors of 1024 or 64, depending on the value of θ.

The decision time was about 100 ns for the fast trigger and 2 μs for the slow logic. The rates and the dead-time of the fast and slow decisions are discussed in subsect. 3.1.

2.4. The data acquisition system

A schematic sketch of the data acquisition system is shown in fig. 5. Following a positive trigger decision, events were read into an on-line computer of the type EMR

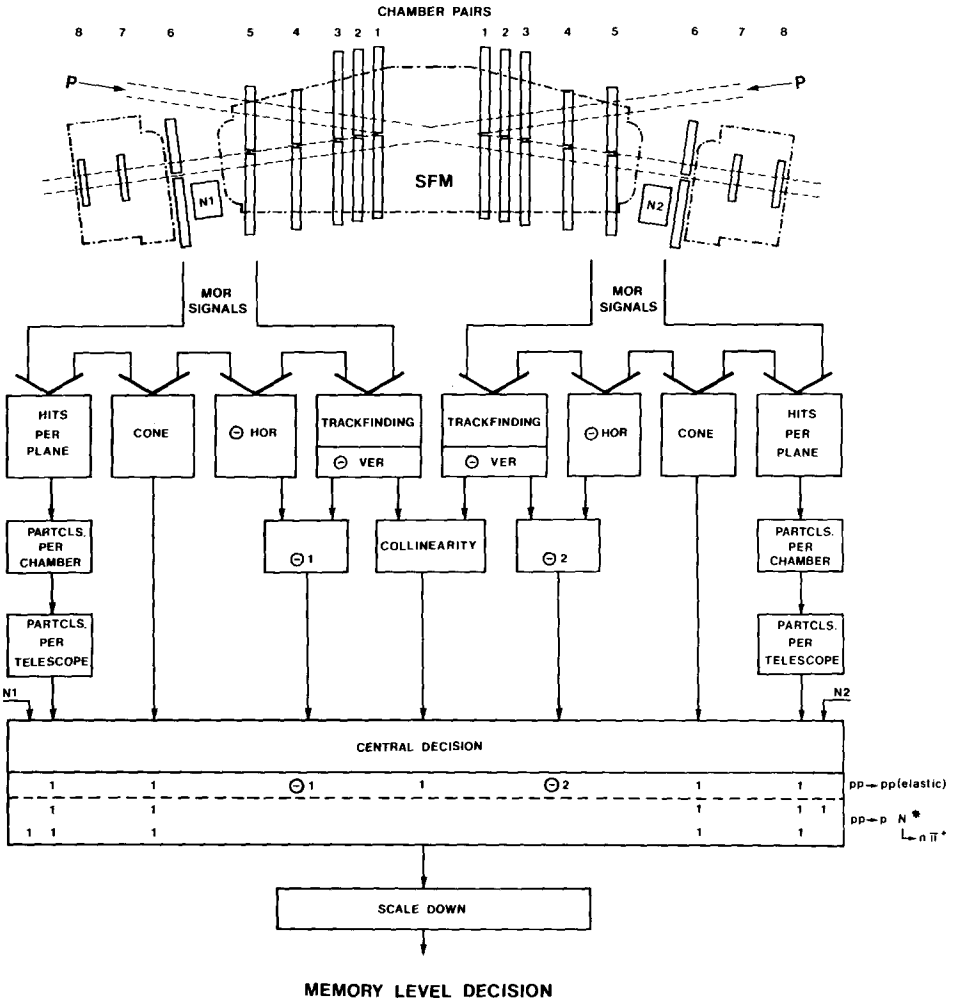

Fig. 4. Schematic diagram of the slow decision logic and its various functions. N1 and N2 are neutron vertex detectors. MOR signifies memory OR.

6130 disposing of a 24 K memory of 16-bit words. It was equipped with a disk unit, two tape units (9 tracks, 1600 bits per inch), and a graphics display; it was connected *via* a link to a large computer of the type CII 10070. For each event, the following information was read in:

(i) The addresses of all wires hit *via* a special data bus and read-out electronics (variable number of 16-bit words, on the average about 100 for elastic scattering triggers).

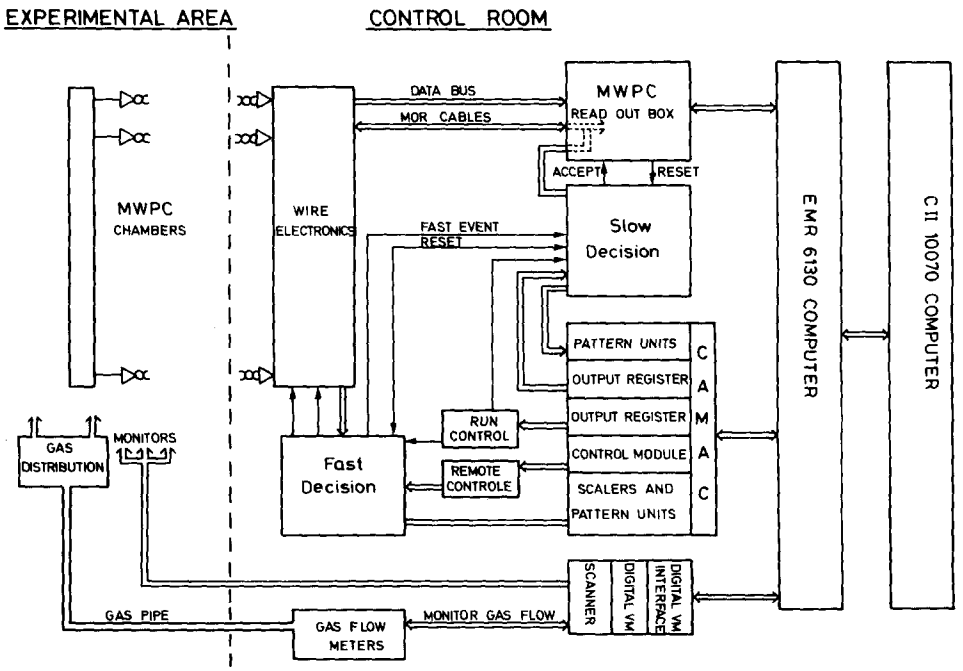

Fig. 5. Schematic diagram of the data acquisition system.

(ii) The content of two CAMAC crates; one crate containing 44 words with monitor rates and fast decision rates, real time and lifetime, time-of-flight information, event type patterns, hit patterns of chamber pairs, and hit patterns of scintillators; and a second crate containing 26 words with counting rates, patterns, and functions of the slow decision logic.

The computer added a third block of seven words per event containing the date, time, run number, and the event number, filled some preselected histograms for equipment monitoring, and wrote the three blocks onto magnetic tape. The tape writing speed limited the data acquisition to about 100 events per second.

In addition to the three data blocks per event, the computer wrote another block of system-control information onto tape at regular intervals of every 10 minutes. On-line histogramming was restricted to, for example, wire hit maps, time-of-flight and scintillator pulse-height distributions. The link to the CII 10070 computer was used to transfer a test sample of events for complete reconstruction. Checks and equipment tests were performed using the EMR computer.

2.5. The luminosity counters

An array of scintillation counters T1 and T2 in each forward telescope, each array covering an area of $1.20 \times 2.00\ m^2$, was placed at a distance of 6 m from the

interaction point as shown in fig. 1. The coincidence rate $N = N(\mathrm{T1} * \mathrm{T2})$, corrected for the accidental rate and gated with the busy signal, was recorded together with each event. It was used as the main luminosity monitor of the experiment. For part of the time, two other scintillator coincidences were used to check the stability of N. The pulse heights of all 20 photomultipliers of these arrays were continuously surveyed.

The absolute calibration of the monitor system was determined using a method due to Van der Meer [18], and was repeated at intervals of a few days. This method consists of counting the monitor rate N as a function of the vertical separation z of the two beams, and of determining the effective overlap height h_{eff}, as defined in eq. (2.1), by the ratio of the integral $\int N \, \mathrm{d}z$ to the maximum value of N. No knowledge of the total cross section is required. The systematic uncertainty of the method is at present estimated to be around 1% [19].

The effective cross sections monitored by the coincidence rate N were found to vary from (20 ± 1) mb at $\sqrt{s}$ = 23 GeV to (31 ± 1.5) mb at $\sqrt{s}$ = 62 GeV and to be stable within ±5% at each energy.

3. The data acquisition and the analysis

3.1. Data taking

A total of 42 million elastic scattering triggers were recorded onto 1658 magnetic tapes, most of the time together with other types of triggers as mentioned in sect. 1. The highest integrated luminosity, $L_{\mathrm{int}} = \int L \, \mathrm{d}t$, was obtained at $\sqrt{s}$ = 53 GeV, where most of the ISR users wanted to accumulate their highest statistics at that time. At the four other energies, lower values of L_{int} were obtained, approximately one tenth of the value at 53 GeV.

The coasting beams have a momentum spread of typically ±1% around their central values. The average c.m. energies $\sqrt{s}$ are shown in table 1. This table also shows the average luminosity and the integrated luminosities, as determined by the luminosity monitor, the number of magnetic tapes and of events recorded, and finally the number of elastic scattering events above $|t| = 0.8$ GeV^2 after all cuts, as discussed in subsect. 3.5. As the accumulated statistics increased, both the fast and the slow decision logics were modified to increase the lower limit of the accepted t-region. Therefore, the number of elastic scattering events is not proportional to L_{int}. During the last runs at $\sqrt{s}$ = 53 GeV, the trigger conditions were set to $|t| \gtrsim 3.3$ GeV^2.

Counting rates and the system dead-time are strongly correlated with the trigger conditions chosen. At $\sqrt{s}$ = 53 GeV and for $L = 5 \times 10^{30}$ cm^{-2} s^{-1}, for example, the fast trigger rate without reference region condition would have been 10^5/s. Including the reference region condition into the fast trigger (see subsect. 2.3), this rate was reduced by a factor of about 10, resulting in a dead-time of the slow decision logic of $10^4/\mathrm{s} \times 2\ \mu\mathrm{s} = 2\%$. The slow decision logic reduced this rate by another

factor of about 200. The data acquisition system requires about 4 ms to read and write an event, resulting in a dead-time of about 50/s × 4 ms = 20%.

3.2. The event reconstruction

The 42 million elastic scattering triggers were passed through a chain of three reconstruction programs:

MARC, associating coordinates to tracks [20],

NICOLE, fitting tracks in the magnetic field and their vertex [21],

KINFIT, performing a kinematical fit for the hypothesis of elastic scattering.

Because of the large amount of data to be processed, the first two standard programs were used in a modified version. NICOLE was used with a parametric method [22], adapted to the wire chamber geometry, and MARC (for the 1976 data only) rejected tracks with too small a scattering angle or too big a curvature, both limits being determined using simulated elastic scattering events.

In spite of these modifications, the total computation load was very high and the event reconstruction work had to be shared between the collaborating laboratories, using essentially identical programs. For the data obtained in 1974, MARC was run on a CDC computer 7600 at CERN, and NICOLE and KINFIT on an IBM 370/168 computer at Hamburg and a CYBER 74 computer at Vienna. The data obtained in 1976 were analysed on an IBM 360/65 computer at Heidelberg. Small samples of events were analysed on two computers for comparison. As far as possible, the book-keeping of the reconstruction work was also computerized.

The fraction of accepted events varied with energy and trigger conditions; typically it was as follows: 20% in MARC, 25% in NICOLE, and 80% in KINFIT. The computation per event took 12 ms in MARC, 35 ms in NICOLE, and 10 ms in KINFIT, of Central Processor time of a CDC 7600.

3.3. The reconstruction programs

The pattern recognition program MARC [20] converted all wire addresses into coordinates and generated space points for each chamber pair, using the additional information of the high-voltage strips. If it was possible to form more than one space point per chamber, an assignment algorithm was used to define the most probable space points, in order to keep the number of spurious points to a minimum [23].

To perform the track finding for elastic scattering, the chambers were assembled into two independent sets in each telescope: all the chambers in the main magnet and a set including chambers at the exit of the main magnet together with the chambers in the compensator magnets. A scan starts by looking first for space points in the most distant chambers of a set. When two outer points were available, they were joined and the following tests were made:

(i) does the vertical track projection point to the beam crossing region?

(ii) can additional points be found, using a parabola test in the horizontal projection, the field map, and rough χ^2 tests?

(iii) does the horizontal projection point to the beam crossing region?

(iv) has the minimum number of required points been found?

This leads to a preliminary definition of a track, and the next search starts. The coordinates of successfully reconstructed tracks were removed. As a last step the search for tracks defined by three coordinates was performed.

For the second set of chambers a similar procedure was applied, but spline curves had to be used to test S-shaped track candidates. Finally, the number of tracks sharing a large proportion of the same space points was reduced and a compatibility code assigned by using a graph theoretical method [24], and a preliminary estimate of the charge and the momentum was made.

The geometry program NICOLE [21] aimed at attaining the limit of the resolution capability of the detector. For all t values of elastic scattering events, the fit procedure had to be as selective as possible. Besides the scattering on the foam-frame of the proportional chambers, a large contribution to multiple scattering was introduced by the walls of the beam tube. The momentum resolution was about ±5% because of the small sagitta at such high momenta. Therefore, full use had to be made of the constraints provided by the equations of motion in the strongly inhomogeneous magnetic field, and the least-squares sum had to be carefully weighted, considering the chamber resolution as well as the multiple scattering [25].

In order to save computer time by avoiding numerical integration of the equations of motion, a parametric method was used [22] in NICOLE. For the track coordinates, which are determined by five parameters in a given reference plane, namely x_r, z_r, $(dx/ds)_r$, $(dz/ds)_r$, and $1/p$, an explicit solution of the dependence on the five parameters was given. This was facilitated by limiting the range of the fifth parameter $1/p$ to the elastic case, imposing energy conservation already at the geometry program level. The fit was performed in two steps to make data reduction more efficient: first the two individual particle paths were fitted, and then they were constrained to fit a common vertex.

The kinematical-fit program KINFIT was specially written for this experiment. Flexible input of the ISR parameters was possible, and the earlier use of the information on energy conservation of both scattered particles was taken into account. KINFIT was therefore essentially a collinearity test with two constraints. Four-momentum conservation was taken into account by applying the Lagrangian method. The problem was linearized, and iterations were continued until convergence was reached.

Fig. 6 shows the observed deviations from collinearity, $\Delta\theta$, in both projections before applying KINFIT. As can be seen, one standard deviation from collinearity is between 1.0 and 1.2 mrad in each projection.

All events with less than 10 standard deviations from collinearity (KINFIT $\chi^2 < 100$) were written onto a data summary tape with the following information: four words of book-keeping; two words of chamber and scintillator patterns; s, t,

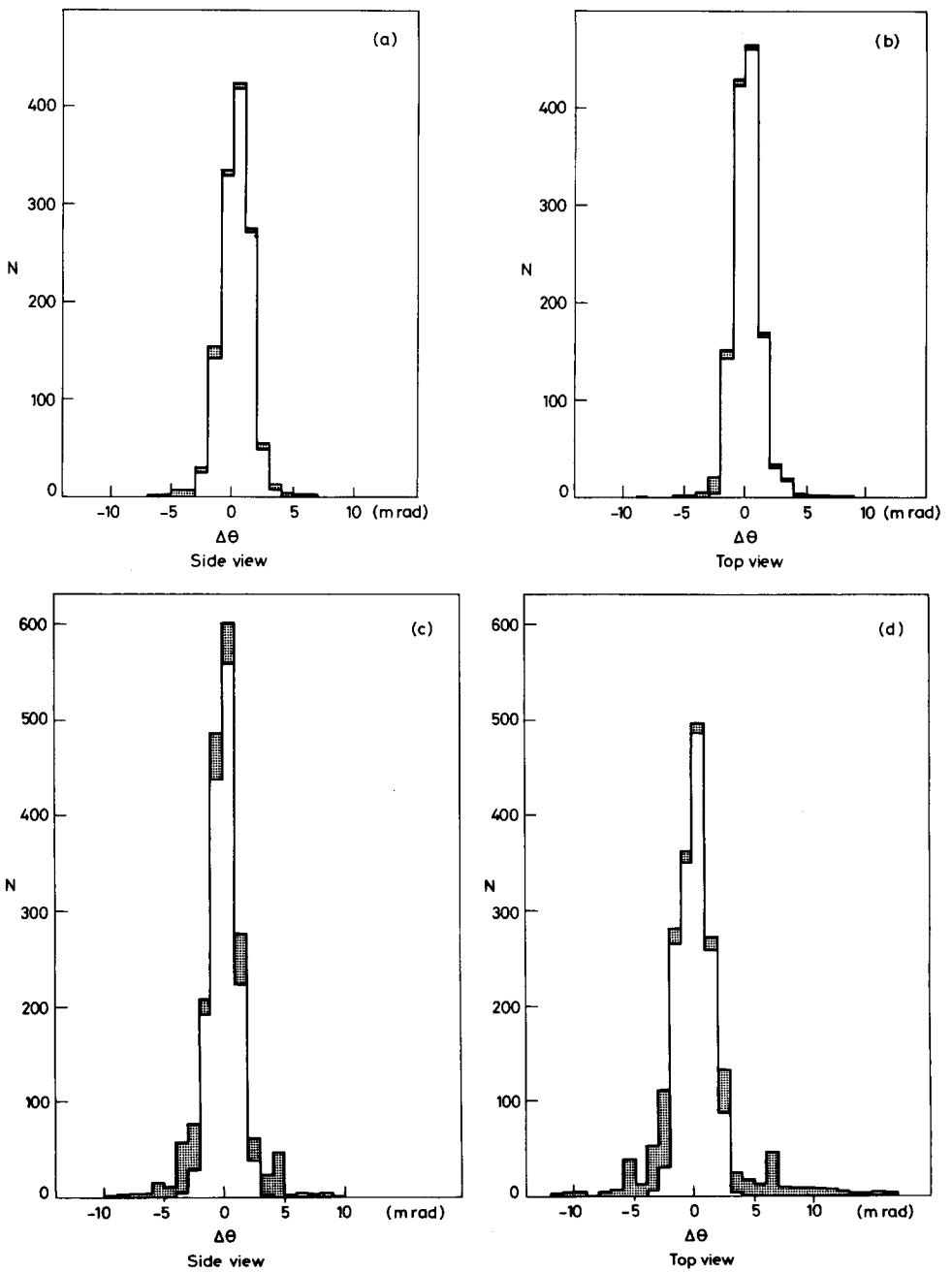

Fig. 6. Deviation from collinearity after track and vertex fitting in the magnet. (a) side view at $\sqrt{s}$ = 23 GeV; (b) top view at 23 GeV; (c) side view at 62 GeV; (d) top view at 62 GeV. The histogram shows events with χ^2(KINFIT) < 9, the shaded areas with $9 < \chi^2 < 100$. The standard deviation is between 1 and 1.2 mrad, compatible with measuring errors.

and the azimuthal scattering angle ϕ; three coordinates of the vertex; and all chamber coordinates of the two tracks.

3.4. Calculation of the acceptance and of the resolution in t

Owing to the inhomogeneous chamber geometry, the trigger conditions, and the absorption of protons in the beam tube and in the proportional chambers and their frames, not all events are detected, and it is therefore required to calculate the overall acceptance which depends on s and t. This has been determined using simulated elastic scattering events generated with the help of the Monte Carlo method. A total of 1.2 million simulated events, on the average 10^4 for each ISR run and each trigger condition, have been generated and treated as realistically as possible.

The simulation took into account the phase-space distribution of the colliding beams, the scattering process following a given t distribution with uniform distribution in azimuthal angle ϕ, and included the tracking of the scattered protons through the magnetic field and the detectors. When traversing material, Coulomb scattering was simulated, and to correct for nuclear elastic and inelastic scattering in the beam tube and in the chamber frames all traversed lengths were recorded. Fig. 7 shows the average thickness $\bar{L}$ of steel traversed for both protons as a function of t.

The simulated events were then processed with the same chain of reconstruction programs as for the real events. Coordinates were transformed into wire addresses, trigger conditions were simulated, and then MARC-NICOLE-KINFIT were applied.

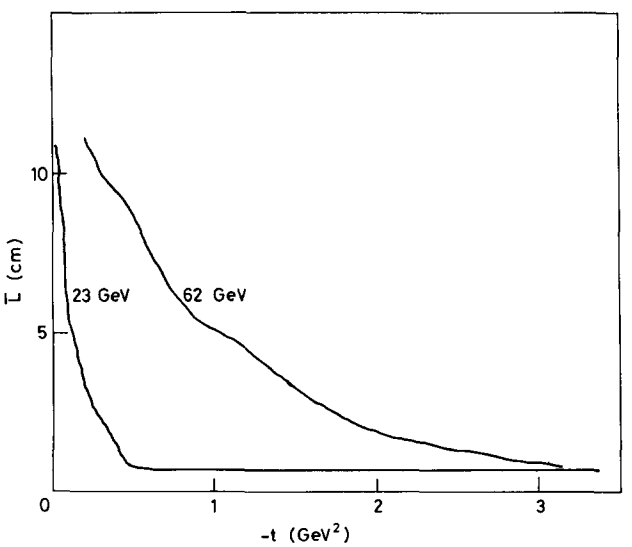

Fig. 7. The average length $\bar{L}$ of vacuum chamber material traversed by both protons.

The resulting data-summary tape contained surviving events and also all rejected events with a flag indicating at which stage they were rejected. The differential cross sections can then be evaluated using the expression

$$\frac{\mathrm{d}\sigma(i)}{\mathrm{d}t} = \frac{\Delta N_{\mathrm{obs}}(i)}{\Delta t} \quad \frac{1}{L_{\mathrm{int}}(i)} \quad \frac{\Delta N_{\mathrm{gen}}(i)}{\Delta \tilde{N}_{\mathrm{acc}}(i)} \tag{3.1}$$

in bins of Δt and $\Delta\phi$ and under various selection criteria for different subsamples i. L_{int} is the integrated luminosity, N_{obs} is the number of real events observed, N_{gen} is the number of simulated events generated, and $\tilde{N}_{\mathrm{acc}}$ is the weighted sum of simulated events accepted, where the weight of each event is given by its survival probability after nuclear elastic and inelastic scattering in the beam tube and in the chamber frames. These weights were determined separately to save computer time. It was, however, ascertained on test samples that this weight method gives the same result as a full simulation.

The final acceptance as a function of t, defined by the event selection procedure (see subsect. 3.5) is shown in fig. 8. Because of different trigger conditions and different cuts for different subsamples i, the acceptance curves are discontinuous; they correspond to an "average" acceptance defined by

$$\eta = \frac{\sum_i L_{\mathrm{int}}(i)\, \Delta \tilde{N}_{\mathrm{acc}}(i)/\Delta N_{\mathrm{gen}}(i)}{\sum_i L_{\mathrm{int}}(i)} \quad . \tag{3.2}$$

The statistical errors on the acceptance follow from binomial distributions. For a discussion of the systematical errors, see subsect. 3.5. The statistical errors of the simulated events in each t bin and for each subsample were always kept below the statistical errors of the corresponding sample of real events and never exceeded 20%.

Simulated events have also been used for trigger studies, for testing the reconstruction programs, and for determining the resolution in t. Fig. 9 shows the t resolution, defined as one standard deviation of the difference between the true and the reconstructed t value in simulated events. At large t, the resolution depends linearly on t and is due to the momentum spread of the ISR beams only.

3.5. The data selection, correction and normalization

Differential cross sections $\mathrm{d}\sigma(i)/\mathrm{d}t$ were obtained from each data subsample by using eq. (3.1) and were compared to each other. Before averaging to obtain

$$\frac{\mathrm{d}\sigma}{\mathrm{d}t}\,(\mathrm{final}) = \frac{\sum_i \Delta N_{\mathrm{obs}}(i)/\Delta t}{\sum_i L_{\mathrm{int}}(i)\, \Delta \tilde{N}_{\mathrm{acc}}(i)/\Delta N_{\mathrm{gen}}(i)} \quad , \tag{3.3}$$

the criteria of selection for each subsample have been determined. The first cut

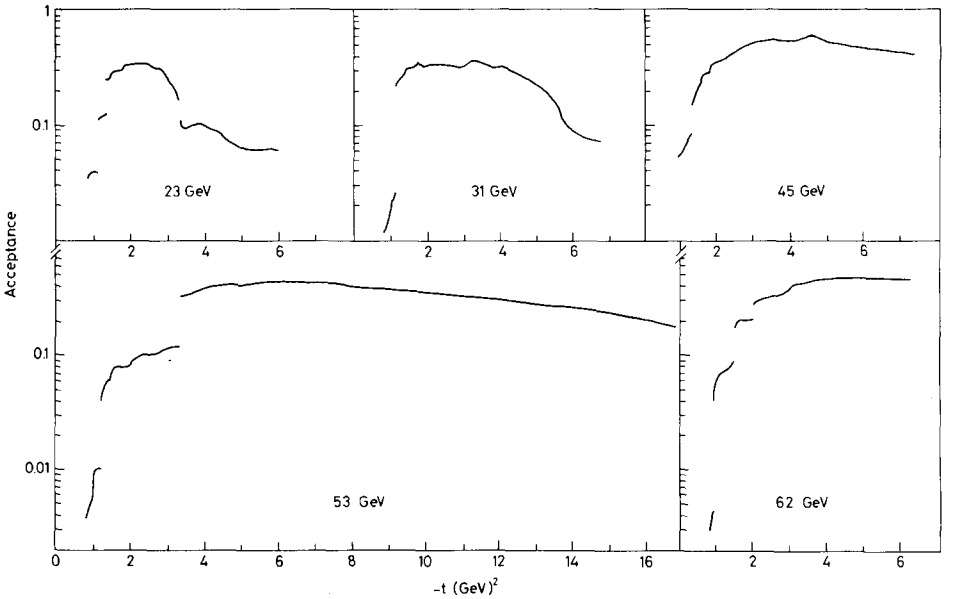

Fig. 8. The acceptance of the detector, the trigger, and of the reconstruction chain. The discontinuities are explained in the text.

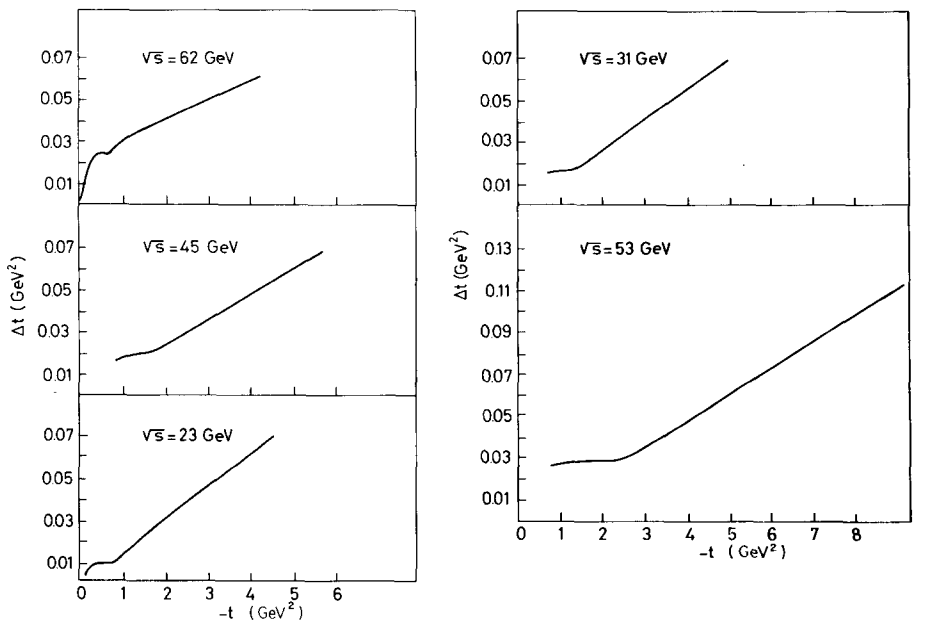

Fig. 9. Calculated experimental resolution in t, defined as one standard deviation of the difference between true and reconstructed t values.

applied to all real and simulated events was aimed at eliminating inefficient regions at the edges of all wire chambers. Using the track-point information on the data-summary tapes, all events were rejected which had not three points, or four points if the actual trigger conditions required four, inside a fiducial region excluding three wires from all edges in each chamber. The remaining chamber inefficiencies were assumed to be uniform over the fiducial region and were determined experimentally by comparing tracks of real and simulated events with 3, 4, and 5 coordinates. They amounted to approximately 1% per chamber and were taken into account by appropriately weighting $\tilde{N}_{acc}$.

Apart from these tests on each event, the following selection criteria were applied:

(a) $\chi^2(\text{KINFIT}) < 9$,

(b) $|t| > 0.8$ GeV^2,

(c) all t regions (per subsample) with $\eta(i) = \Delta\tilde{N}_{acc}/\Delta N_{gen} < 0.10$ were rejected,

(d) some subsamples were also cut in the azimuthal angle ϕ if the shape of the distributions of $dN_{obs}/d\phi$ and $d\tilde{N}_{acc}/d\phi$ did not agree with each other.

The distributions in azimuthal angle ϕ were extensively studied and were an essential tool for checking the quality of the data. Fig. 10 shows an example of the azimuthal asymmetry between observed and accepted Monte Carlo events, $R = (dN_{obs} - d\tilde{N}_{acc})/(dN_{obs} + d\tilde{N}_{acc})$ for $\sqrt{s} = 45$ GeV and for the t interval from 1 to 1.2 GeV^2.

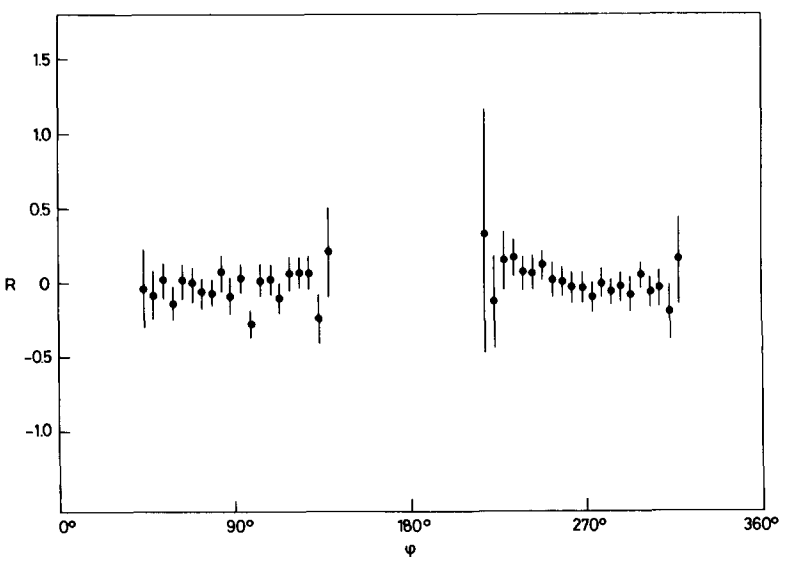

Fig. 10. Example of a distribution of the azimuthal asymmetry between observed and accepted Monte Carlo events, $R = (dN_{obs} - d\tilde{N}_{acc})/(dN_{obs} + d\tilde{N}_{acc})$ at $\sqrt{s} = 45$ GeV and in the t interval 1 to 1.2 GeV^2.

There remain two uncertainties at the 3% to 5% level which are not included in the acceptance calculation:

(i) The effects of δ-rays in the wire chambers. They lead to clusters of hit wires which are much larger than the average cluster size of ≈1.5, and to the loss of the track coordinate.

(ii) Inelastic scattering of a proton in an obstacle after having properly traversed three or more wire chambers. This simulates a high multiplicity event which may be rejected by the slow decision logic.

Both effects have been studied using the data [26], and a resulting correction factor of 1.08 ± 0.04 was applied to $\Delta\tilde{N}_{\mathrm{acc}}$.

Another source of systematical uncertainty, already mentioned in subsect. 3.4 and illustrated in fig. 7, is the amount of beam-tube material traversed. Because of approximations, the calculated values of $\bar{L}$ may have an uncertainty of up to 20%, and this has also been included into the errors of $\Delta\tilde{N}_{\mathrm{acc}}$.

The absolute normalization of the data is determined by the integrated luminosities $L_{\mathrm{int}}(i)$. They are determined by the monitor counters, using the calibration procedure as described in subsect. 2.5. From the reproducibility of the monitor cross sections and from the comparison of $\mathrm{d}\sigma(i)/\mathrm{d}t$ of different subsamples the systematic error on $\mathrm{d}\sigma(\mathrm{final})/\mathrm{d}t$ due to normalization uncertainties is estimated to ±5%.

3.6. Estimation of the background

The procedure of determining the background is illustrated in fig. 11. The distribution of χ^2 for the kinematical fit to the experimental data, shown as full circles in the figure, is well-described by an expression

$$P(\chi^2) = \mathrm{e}^{-f\chi^2/2}. \tag{3.4}$$

Since the kinematical fit has two essential degrees of freedom we expect a distribution described by $\mathrm{e}^{-\chi^2/2}$, shown as the dashed curve in fig. 11. Owing to the neglect of many randomly distributed uncertainties, e.g., alignment errors, f is slightly smaller than 1, and up to $\chi^2 = 10$ it turns out to be about 0.8, as shown by the full line. For higher values of χ^2, there is a strong deviation from eq. (3.4). As the expected number of events due to nuclear elastic scattering in the beam tube does not exceed 20% of all events in this χ^2 region, as shown by open squares, we attribute this deviation mainly to the background of non-elastic scattering events. Extrapolating the χ^2 distribution from the region of $\chi^2 > 20$ to the region of $\chi^2 < 9$, as also shown in the figure, we can estimate the minimum and maximum amount of background under the elastic peak.

This procedure was carried out for all ISR energies and for several t intervals, and allows us to draw the following conclusions.

The background level is generally of the order of (4 ± 2)%, as shown in fig. 12 for $\sqrt{s} = 31$ GeV. The number of real events lost by the selection criterion $\chi^2 < 9$ is about 4% higher than for simulated events for which $f = 1$. The two corrections

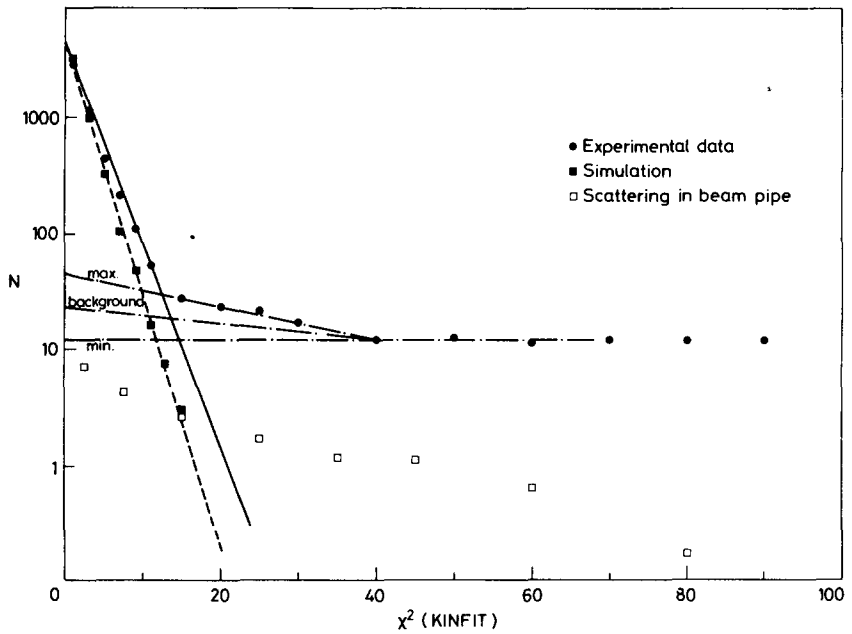

Fig. 11. Example of a χ^2 distribution of the kinematical fit for observed and for simulated events. The contribution of diffraction scattering in the beam tube is also shown. The distribution of simulated events is described by $\exp(-\frac{1}{2}\chi^2)$ as expected for 2 degrees of freedom (dashed curve), whereas the observed events follow a distribution described by $\exp(-0.8\chi^2/2)$ owing to the neglect of some randomly distributed uncertainties. An estimate of the minimum and the maximum background is obtained by extrapolating the tail at large χ^2 towards $\chi^2 = 0$.

cancel each other and therefore no background subtraction has been made in $d\sigma/dt$.

In the t region between 0.8 and 5 GeV^2, the background can be well-approximated by the function:

$$d\sigma(\text{background})/dt = \alpha \exp[-\beta(|t| - 1.425\ \text{GeV}^2)] , \qquad (3.5)$$

where $\alpha = (1 \pm 0.5)$ nb/GeV^2 and $\beta = (1.8 \pm 0.2)$ GeV^{-2} are independent of the energy.

At higher t values the background may increase slightly but always remains smaller than 10% of the signal.

Hence, background is always negligible except in the narrow t region around the diffraction minimum. However, even in the bin with the lowest cross section, at $\sqrt{s} = 31$ GeV and in the t interval from 1.40 to 1.45 GeV^2, the background level is lower than the number of observed events, as shown in fig. 13. It is estimated at (40 ± 20)%, in agreement with eq. (3.5).

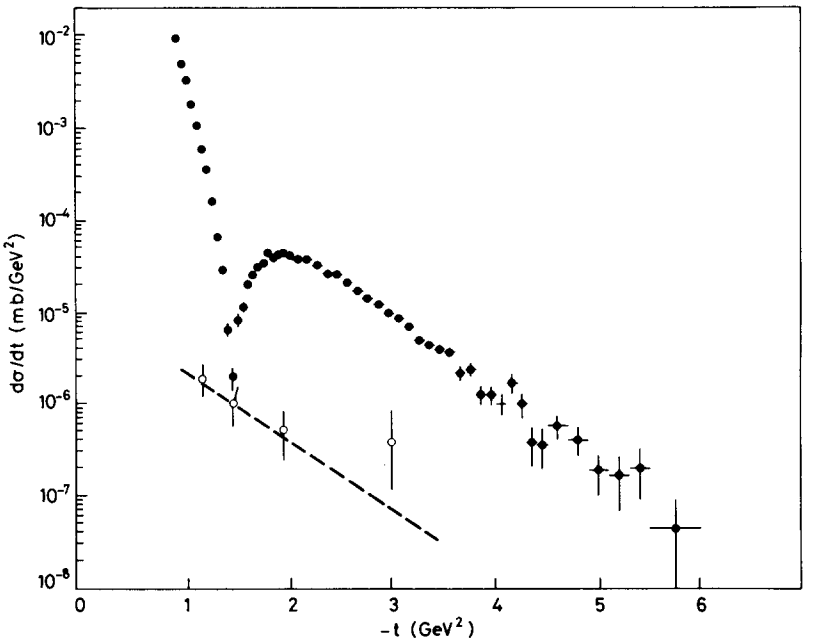

Fig. 12. Differential cross section and estimated background (open circles) at $\sqrt{s}$ = 31 GeV. The background is (4 ± 2)% except near the minimum.

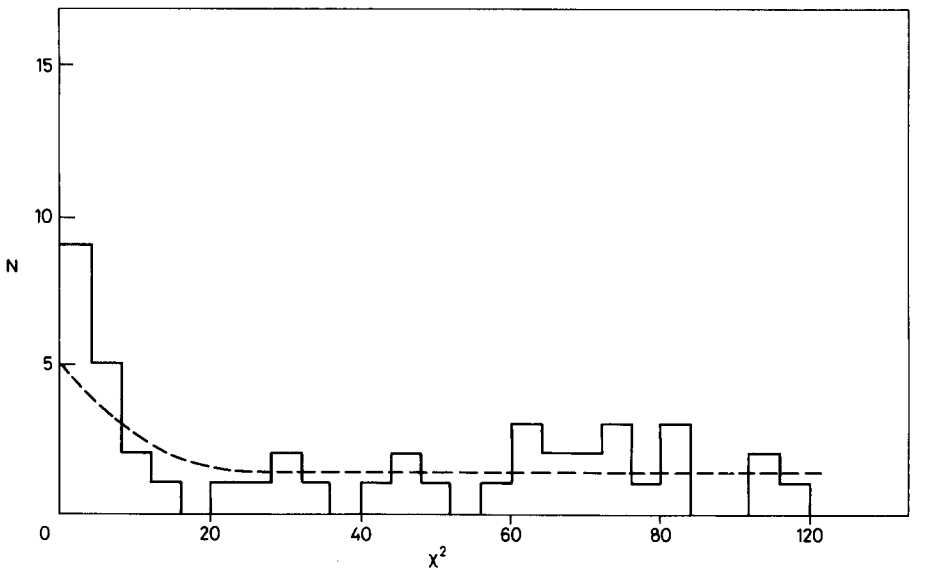

Fig. 13. χ^2 distribution of events in the t bin around the diffraction minimum at $\sqrt{s}$ = 31 GeV. The dotted curve corresponds to the best estimate of the background level as demonstrated in fig. 11. We find a ratio of background-to-signal of (40 ± 20)%.

Table 2
Differential cross sections, $d\sigma/dt$ in (mb/GeV^2)

t (GeV^2)	dt (GeV^2)	$\sqrt{s}$ = 23.4 GeV	$\sqrt{s}$ = 30.5 GeV	$\sqrt{s}$ = 44.6 GeV	$\sqrt{s}$ = 52.8 GeV	$\sqrt{s}$ = 62.1 GeV
			$d\sigma/dt$ (mb/GeV^2) (and relative error (%))			
0.825	0.050	1.67E-02 (6)			1.12E-02 (13)	1.02E-02 (16)
0.875	0.050	9.88E-03 (6)	9.53E-03 (8)	6.81E-03 (15)	6.16E-03 (13)	5.67E-03 (15)
0.925	0.050	6.08E-03 (6)	5.19E-03 (7)	4.23E-03 (13)	4.76E-03 (19)	3.05E-03 (17)
0.975	0.050	3.72E-03 (6)	3.32E-03 (7)	2.10E-03 (10)	1.93E-03 (16)	1.54E-03 (17)
1.025	0.050	2.36E-03 (6)	1.93E-03 (6)	1.17E-03 (9)	9.16E-04 (18)	7.17E-04 (15)
1.075	0.050	1.32E-03 (6)	1.07E-03 (7)	6.77E-04 (9)	5.87E-04 (18)	4.44E-04 (16)
1.125	0.050	8.12E-04 (6)	5.96E-04 (7)	3.56E-04 (10)	3.97E-04 (19)	1.80E-04 (16)
1.175	0.050	4.30E-04 (6)	3.58E-04 (7)	1.62E-04 (10)	1.32E-04 (16)	9.41E-05 (18)
1.225	0.050	1.97E-04 (9)	1.58E-04 (7)	9.08E-05 (9)	5.76E-05 (10)	6.12E-05 (18)
1.275	0.050	1.01E-04 (10)	6.67E-05 (8)	4.17E-05 (10)	3.96E-05 (11)	3.12E-05 (22)
1.325	0.050	4.76E-05 (8)	2.92E-05 (10)	2.31E-05 (12)	2.49E-05 (12)	2.17E-05 (24)
1.375	0.050	2.24E-05 (11)	6.38E-06 (17)	1.31E-05 (15)	2.25E-05 (10)	3.89E-05 (19)
1.425	0.050	4.73E-06 (20)	2.00E-06 (28)	2.07E-05 (12)	2.91E-05 (11)	2.56E-05 (20)
1.475	0.050	8.67E-06 (15)	8.28E-06 (15)	2.41E-05 (11)	3.20E-05 (9)	4.86E-05 (18)
1.525	0.050	1.27E-05 (13)	1.17E-05 (12)	3.35E-05 (10)	4.21E-05 (8)	3.78E-05 (14)
1.575	0.050	2.24E-05 (10)	2.04E-05 (10)	3.78E-05 (9)	4.63E-05 (8)	4.80E-05 (13)
1.625	0.050	2.80E-05 (10)	2.51E-05 (10)	4.62E-05 (9)	4.93E-05 (8)	4.44E-05 (13)
1.675	0.050	3.21E-05 (9)	2.97E-05 (9)	4.69E-05 (9)	5.58E-05 (8)	5.55E-05 (12)
1.725	0.050	3.98E-05 (9)	3.43E-05 (8)	5.47E-05 (8)	5.95E-05 (8)	6.62E-05 (12)
1.775	0.050	3.93E-05 (8)	4.42E-05 (8)	4.77E-05 (8)	5.93E-05 (7)	5.59E-05 (12)
1.825	0.050	4.51E-05 (8)	3.95E-05 (9)	5.70E-05 (8)	5.98E-05 (7)	6.50E-05 (12)
1.875	0.050	4.52E-05 (8)	4.25E-05 (9)	4.85E-05 (8)	5.59E-05 (7)	6.54E-05 (11)
1.925	0.050	4.58E-05 (8)	4.39E-05 (8)	5.40E-05 (8)	5.77E-05 (7)	5.74E-05 (12)
1.975	0.050	4.26E-05 (8)	4.28E-05 (9)	5.35E-05 (8)	5.58E-05 (7)	5.03E-05 (13)
2.050	0.100	4.50E-05 (6)	3.71E-05 (7)	5.11E-05 (6)	5.19E-05 (6)	4.09E-05 (9)
2.150	0.100	4.08E-05 (6)	3.70E-05 (7)	3.94E-05 (7)	4.57E-05 (6)	4.12E-05 (9)
2.250	0.100	3.22E-05 (7)	3.19E-05 (7)	2.88E-05 (7)	3.61E-05 (6)	3.37E-05 (9)
2.350	0.100	2.77E-05 (7)	2.65E-05 (7)	2.87E-05 (7)	3.16E-05 (6)	3.11E-05 (9)

2.450	0.100	2.33E-05 (7)	2.61E-05 (7)	2.42E-05 (7)	2.62E-05 (6)	2.48E-05 (9)
2.550	0.100	1.97E-05 (8)	2.14E-05 (8)	2.15E-05 (7)	2.28E-05 (6)	2.07E-05 (10)
2.650	0.100	1.80E-05 (8)	1.69E-05 (9)	1.68E-05 (7)	1.84E-05 (6)	1.74E-05 (10)
2.750	0.100	1.29E-05 (9)	1.41E-05 (9)	1.59E-05 (8)	1.61E-05 (6)	1.31E-05 (11)
2.850	0.100	1.15E-05 (10)	1.24E-05 (9)	1.34E-05 (8)	1.37E-05 (6)	1.12E-05 (12)
2.950	0.100	1.02E-05 (11)	9.65E-06 (11)	1.06E-05 (8)	1.04E-05 (7)	1.06E-05 (12)
3.050	0.100	1.22E-05 (11)	8.60E-06 (10)	7.36E-06 (10)	8.63E-06 (7)	7.20E-06 (13)
3.150	0.100	6.16E-06 (15)	7.05E-06 (11)	6.96E-06 (10)	6.88E-06 (7)	5.63E-06 (14)
3.250	0.100	6.61E-06 (16)	4.94E-06 (13)	4.61E-06 (12)	5.66E-06 (8)	5.64E-06 (14)
3.350	0.100	4.90E-06 (24)	4.45E-06 (14)	5.20E-06 (12)	4.82E-06 (6)	5.43E-06 (15)
3.450	0.100	7.34E-06 (21)	3.97E-06 (14)	4.01E-06 (12)	4.66E-06 (6)	3.13E-06 (18)
3.550	0.100	5.07E-06 (25)	3.69E-06 (15)	3.68E-06 (13)	3.55E-06 (6)	3.27E-06 (18)
3.650	0.100	2.93E-06 (31)	2.27E-06 (19)	3.08E-06 (13)	3.03E-06 (6)	2.86E-06 (19)
3.720	0.100	4.18E-06 (26)	2.46E-06 (19)	2.03E-06 (16)	2.23E-06 (6)	2.48E-06 (20)
3.850	0.100	1.81E-06 (39)	1.28E-06 (25)	1.82E-06 (17)	1.91E-06 (7)	2.72E-06 (18)
3.950	0.100	2.29E-06 (37)	1.27E-06 (25)	1.89E-06 (17)	1.50E-06 (7)	1.62E-06 (24)
4.050	0.100	1.43E-06 (42)	1.02E-06 (28)	1.67E-06 (18)	1.46E-06 (8)	1.03E-06 (31)
4.150	0.100	1.33E-06 (49)	1.71E-06 (23)	1.22E-06 (20)	1.17E-06 (8)	1.29E-06 (27)
4.250	0.100	5.82E-07 (71)	1.01E-06 (30)	7.25E-07 (26)	1.01E-06 (9)	7.82E-07 (32)
4.350	0.100	7.16E-07 (66)	3.86E-07 (46)	8.95E-07 (24)	7.85E-07 (10)	6.91E-07 (37)
4.450	0.100	8.00E-07 (61)	3.63E-07 (46)	8.59E-07 (23)	6.70E-07 (10)	5.88E-07 (37)
4.600	0.200	4.13E-07 (71)	5.70E-07 (29)	7.13E-07 (20)	5.18E-07 (8)	3.56E-07 (34)
4.800	0.200	7.70E-07 (51)	4.19E-07 (34)	3.31E-07 (29)	3.33E-07 (10)	2.83E-07 (39)
5.000	0.200	6.34E-07 (59)	1.87E-07 (51)	3.14E-07 (31)	2.75E-07 (11)	2.62E-07 (47)
5.200	0.200	6.29E-07 (59)	1.73E-07 (58)	2.08E-07 (34)	2.02E-07 (12)	1.75E-07 (46)
5.400	0.200	4.35E-07 (72)	2.02E-07 (59)	1.31E-07 (46)	1.61E-07 (13)	1.60E-07 (52)
5.750	0.500	9.07E-08 (99)	4.46E-08 (99)	7.02E-08 (38)	8.18E-08 (11)	1.28E-07 (37)
6.250	0.500			4.41E-08 (52)	3.75E-08 (17)	3.20E-08 (71)
6.750	0.500			4.65E-08 (51)	1.54E-08 (26)	
7.250	0.500			1.18E-08 (99)	1.02E-08 (32)	
7.750	0.500				3.22E-09 (58)	
8.250	0.500				4.45E-09 (50)	
8.750	0.500				2.31E-09 (71)	
9.250	0.500				4.59E-09 (50)	
9.750	0.500				3.71E-09 (58)	

The influence of bin size, t resolution, and background is negligible everywhere except at the diffraction minimum. See table 3 for $d\sigma/dt$ (t_{min}). The relative errors expressed in per cent are given in parentheses; they do not include the normalization uncertainty of ±5%.

4. The results

4.1. The differential cross sections

The final results of the differential cross sections $d\sigma/dt$ are given in table 2 and shown in fig. 14. We note the following prominent features.

In the t interval from $t = 0$ to $t = -0.8$ GeV^2, the cross section is rather structureless [10] and decreases approximately as an exponential over four orders of magnitude. It continues to decrease over another three decades until it reaches a pronounced minimum, which is s-dependent in position and depth.

A second maximum is reached at $t \approx -1.9$ GeV^2, and the following exponential

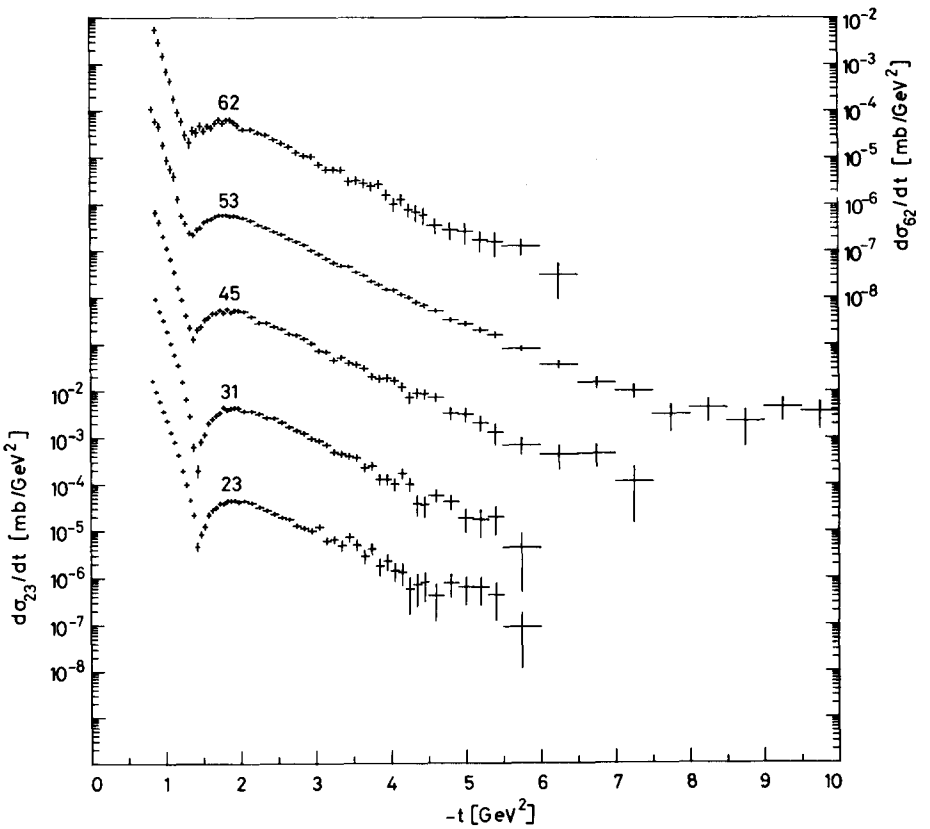

Fig. 14. Final results of the differential cross sections. The five different curves are displaced by a factor of 100 from each other. The left-side scale is valid for $\sqrt{s}$ = 23 GeV, the right-side scale for $\sqrt{s}$ = 62 GeV. For the influence of t resolution and for the background at the minimum, see subsect. 4.3.

decrease is characterized by a much smaller slope than at the forward peak. This slope is constant over nearly three decades. At $\sqrt{s} = 53$ GeV there is a further change of slope near $t = -6$ GeV^2. However, we find no evidence for a second minimum in the t range up to 10 GeV^2.

The errors quoted on the cross sections are evaluated as the sum of the squares of the statistical errors of the experimental data, of the statistical errors in the acceptance calculation, and of the estimated systematic uncertainties. The systematic errors are not independent from one t bin to the other; they include uncertainties originating from δ-rays, from event losses in the slow decision logic, and from the beam-tube traversal. The overall scale error, estimated to be ±5% at each energy, is not included.

Corrections due to the background, the finite bin size, and the influence of the t resolution are negligible everywhere except in the region of the diffraction minimum. Fig. 14 and table 2 give the measured values also there; for the subtraction of the background and the unfolding of the effect due to binning and the t resolution, the reader is referred to subsect. 4.3.

4.2. The forward peak

The data with t values above 0.8 GeV^2 extend over the last three of the seven decades of the forward peak. The value of the slope $b = (\mathrm{d}/\mathrm{d}t)\ \ln(\mathrm{d}\sigma/\mathrm{d}t)$ is known to depend on t in this t region [1]; it is steadily decreasing until a t value of 0.8 GeV^2 is reached, and is approximately compatible [27] with a parametrization of the form $\mathrm{d}\sigma/\mathrm{d}t \propto \exp(bt + ct^2)$. For t values above 0.8 GeV^2, we observe again an increase of the slope. We do not attribute this to a property of the forward amplitude but rather to its destructive interference with a second amplitude. Slope fits have to take this interference into account. We refer to subsect. 4.3 for a discussion. The last column of table 3 gives the slope values derived from a fit including interference. For t values between 0.8 GeV^2 and the diffraction minimum, it is found that the forward peak continues to shrink with increasing energy. This shrinkage is compatible with an energy-independent ratio of b/σ_{T}.

4.3. The diffraction minimum

In order to determine the position and the depth of the observed minimum in the differential cross section, we have fitted a function of the form

$$\frac{\Delta\sigma}{\Delta t}(t') = \frac{1}{\Delta t}\int \mathrm{d}t' \int \frac{\mathrm{d}\sigma}{\mathrm{d}t}(t)\,\frac{\exp[-(t-t')^2/2\delta^2]}{\sqrt{2\pi\delta^2}}\,\mathrm{d}t + bg\,, \tag{4.1}$$

to the observed cross sections at each energy, where δ is the standard deviation of the resolution in t and the background term bg is given by eq. (3.5). The true cross section is parametrized by an expression with two amplitudes described by five

Table 3
Parameters of an expression with two amplitudes [eq. (4.2)], describing $d\sigma/dt$ near the minimum (t interval from 1.05–2.5 GeV^2) as determined by fitting the data

$\sqrt{s}$ (GeV)	t resolution, δ (GeV^2)	Δt_{syst} (GeV^2)	χ^2 for 20 d.f.	t_0 [a] (GeV^2)	t_{min} [b] (GeV^2)	$\frac{d\sigma}{dt}(t_{min})$ (nb/GeV^2)
23.4	±0.020	±0.008	20.6	1.437 ± 0.003	1.440 ± 0.003	4.0 ± 0.9
30.5	±0.020	±0.010	15.9	1.418 ± 0.003	1.418 ± 0.003	$0.5 \pm \frac{0.7}{0.5}$
44.6	±0.020	±0.015	22.2	1.361 ± 0.005	1.370 ± 0.005	13.4 ± 1.5
52.8	±0.030	±0.017	13.7	1.337 ± 0.006	1.348 ± 0.006	19.8 ± 1.9
62.1	±0.035	±0.020	19.2	1.306 ± 0.012	1.322 ± 0.012	22.6 ± 3.7

$\lvert\epsilon\rvert$ [c] (rad)	b [d] (GeV^{-2})	d [d] (GeV^{-2})	B [e] (GeV^{-2})
0.12 ± 0.02	7.2 ± 0.4	2.27 ± 0.24	7.90 ± 0.12
0.06 ± 0.06	8.0 ± 0.4	1.73 ± 0.21	7.85 ± 0.12
0.21 ± 0.04	7.2 ± 0.6	2.26 ± 0.30	8.17 ± 0.19
0.25 ± 0.06	7.0 ± 0.8	2.10 ± 0.36	8.29 ± 0.18
0.34 ± 0.10	7.9 ± 1.2	1.79 ± 0.51	8.66 ± 0.33

[a] t_0 is the minimum position calculated assuming Re f/Im f = 0.
[b] t_{min} is the fitted position of the minimum.
[c] $\pi + \epsilon$ is the phase difference of the interfering amplitudes; $\epsilon = 0$ for destructive interference, Re $f = 0$.
[d] Slope parameters of the two amplitudes.
[e] B is the slope value for a fit to a t interval from 0.8 to 5.1 GeV^2. Owing to smaller errors than on b, it shows the shrinking property mentioned in subsect. 4.2.

parameters [28] at each energy:

$$\frac{d\sigma}{dt} = A\left|e^{b(t-t_0)/2} + e^{d(t-t_0)/2+i\phi}\right|^2 . \tag{4.2}$$

The observed minimum implies that destructive interference occurs and hence that $\phi \approx \pi$. If ϕ were equal to π, e.g., if both amplitudes were purely imaginary, the cross section would be zero at $t = t_0$. If real parts were contributing, we could have $\phi = \pi + \epsilon$, and the minimum would no longer occur at $t = t_0$ but at t_{min} and the

cross section would not go to zero;

$$|t_{\min}| \approx |t_0| + \frac{b+d}{2(b-d)^2}\,\epsilon^2\,, \qquad (4.3)$$

$$\frac{\mathrm{d}\sigma}{\mathrm{d}t}(t_{\min}) \approx A\epsilon^2\,.$$

Eq. (4.2) describes the data reasonably well over a wide t region. To be as model-independent as possible, we have chosen the t interval from 1.05 to 2.5 GeV^2 in which we find good χ^2 values of the fits for the data at all five energies.

The results of the fit are summarized in table 3. The errors quoted for t_0 and $t_{\min}$ are of statistical origin and represent one standard deviation from the fit. In addition, the values of t_0 and $t_{\min}$ are affected by systematic errors owing to the alignment uncertainty of the detectors; these errors are also given in table 3 and are estimated to be $\Delta t_{\mathrm{syst}} = \pm 3 \times 10^{-4}$ GeV $\sqrt{s}$. The errors on the values of $(\mathrm{d}\sigma/\mathrm{d}t)t_{\min}$ and on ϵ contain statistical fitting errors, uncertainty due to background, and a normalization uncertainty of ±5%; the errors on the values of b and d are statistical fitting errors. It has been verified that the best fit values of t_0, $t_{\min}$, $(\mathrm{d}\sigma/\mathrm{d}t)_{\min}$, and ϵ are not sensitive to small variations of the t range chosen for the fit.

The observed s dependence of the position of the minimum is shown in fig. 15. The s dependence is nearly compatible with the one observed for the values of $1/\sigma_{\mathrm{tot}}(\mathrm{pp})$, as expected for diffraction by an object with a radius which is increasing proportionally to $\sqrt{\sigma_{\mathrm{tot}}}$.

The differential cross section at the diffraction minimum as a function of $\sqrt{s}$ is shown in fig. 16. It is observed to decrease as $\sqrt{s}$ is increasing towards 30 GeV, to vanish near $\sqrt{s}$ = 30 GeV, and to increase again. This energy dependence is similar to that of the quantity $\rho^2\sigma_{\mathrm{T}}^2$, where ρ is the ratio of the real to the imaginary part of the scattering amplitude at $t = 0$. The full curve in fig. 16 is proportional to $\rho^2\sigma_{\mathrm{T}}^2$ and has been normalized to the data at $\sqrt{s}$ = 53 GeV. The shaded area around the curve is indicating the statistical errors on $\rho^2\sigma_{\mathrm{T}}^2$ as quoted in refs. [19,29]. We note that the differential cross section at the minimum is proportional to $\rho^2\sigma_{\mathrm{T}}^2$ for $\sqrt{s} > 30$ GeV. This property can be described by the notion of geometrical scaling of the amplitude as discussed in subsect. 5.4.

4.4. The second maximum

Position and height of the second maximum are s dependent too. Best values for these parameters have been determined by fitting quadratic parabolae to the cross section over seven to nine t bins. The values thus determined are given in table 4 and shown in fig. 17. The errors on the values of $t_{\max}$ are of statistical origin since the systematical alignment uncertainty is negligible; the errors on $(\mathrm{d}\sigma/\mathrm{d}t)_{\max}$ contain in addition the normalization uncertainties of ±5%. The curves shown in the figure are proportional to $1/\sigma_{\mathrm{tot}}$ for $t_{\max}$ and to σ_{tot}^2 for $(\mathrm{d}\sigma/\mathrm{d}t)\,t_{\max}$; their meaning will be discussed in subsect. 5.4.

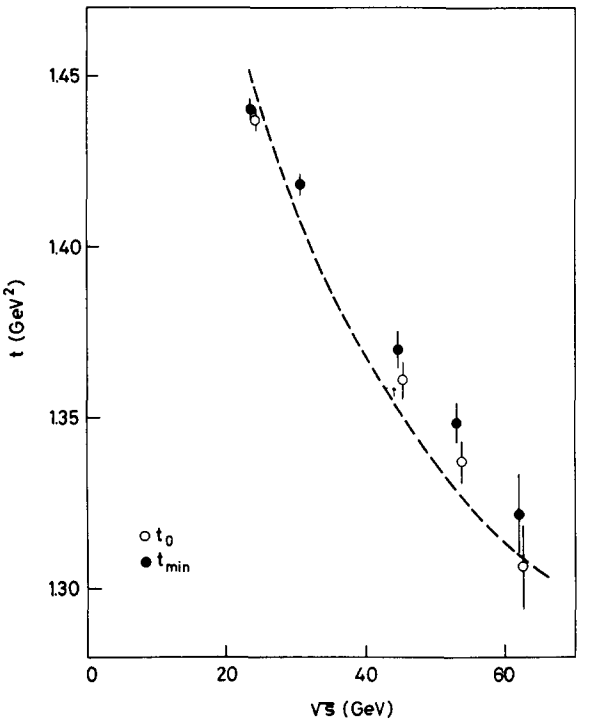

Fig. 15. Observed position of the diffraction minimum as a function of the energy $\sqrt{s}$. Errors are statistical only. t_{min} is the observed t value of the minimum, t_0 the value calculated assuming zero real part of the scattering amplitude. The curve is proportional to the values of $(1/\sigma_{tot})$ of ref. [52].

4.5. The t region beyond the second maximum

Beyond the second maximum, the differential cross section again shows a simple exponential behaviour at all five energies. At each energy, we have tried to find which is the largest t range permitting a good fit to an exponential form

$$\frac{d\sigma}{dt} = C \exp[-D(|t| - 3\ \mathrm{GeV}^2)] \ , \tag{4.4}$$

and have obtained good results in the t interval from 2.3 to 5.1 GeV^2; $|t| = 3$ GeV^2 has been chosen to minimize correlations between the values of the parameters C and D. The results are shown in fig. 18 and in table 5. The errors on D are of purely statistical origin and the errors on C include the normalization uncertainties of ±5%.

The values of the parameters C and D are remarkably energy independent. We have therefore again fitted the data sets at all five energies using common values for

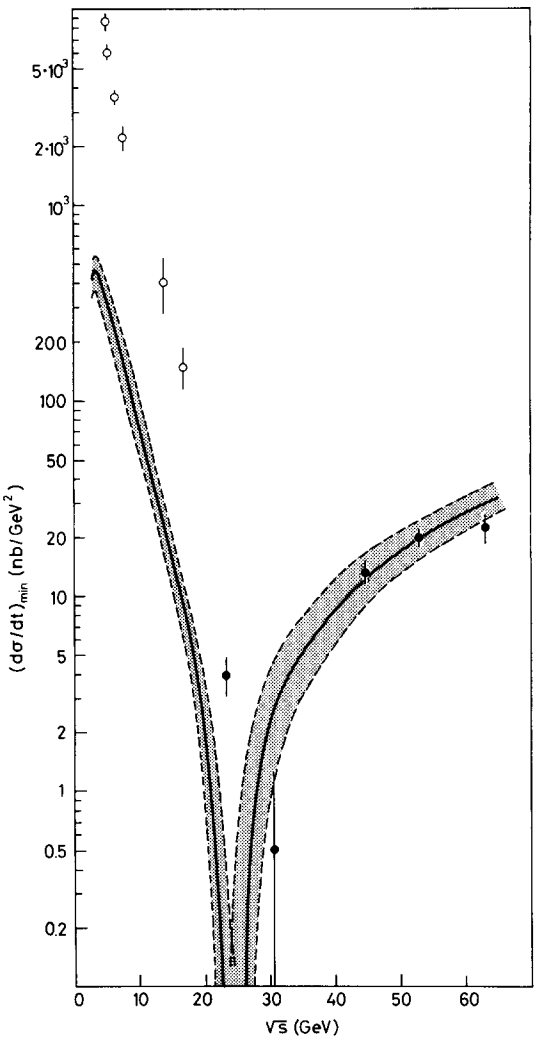

Fig. 16. Energy dependence of the differential cross section at the minimum corrected for background and t resolution. The open data points give the differential cross section at $t \approx -1.4$ GeV^2 as quoted in ref. [39]. The full curve is proportional to $\rho^2\sigma_T^2$ and has been normalized to the data at $\sqrt{s} = 53$ GeV. Values of $\rho = \mathrm{Re}\, f/\mathrm{Im}\, f$ at $t = 0$ are from refs. [19,29]. The shaded area around the full curve is indicating statistical errors on $\rho^2\sigma_T^2$.

C and D in eq. (4.4), and taking into account the ±5% normalization freedom. The fit is good everywhere, and the best values are given at the bottom of table 5 and are shown as solid lines in fig. 18. The dashed curves will be discussed in subsect. 5.4.

Beyond $|t| = 5$ GeV^2, only the data at 53 GeV have enough statistics to deter-

Table 4
Position and differential cross section of the second maximum

$\sqrt{s}$ (GeV)	t (max) (GeV^2)	$\frac{d\sigma}{dt}$ (max) (nb/GeV^2)
23.4	1.97 ± 0.03	45 ± 3
30.5	1.93 ± 0.03	42 ± 3
44.6	1.92 ± 0.10	52 ± 3
52.8	1.81 ± 0.07	58 ± 3
62.1	1.81 ± 0.06	63 ± 5

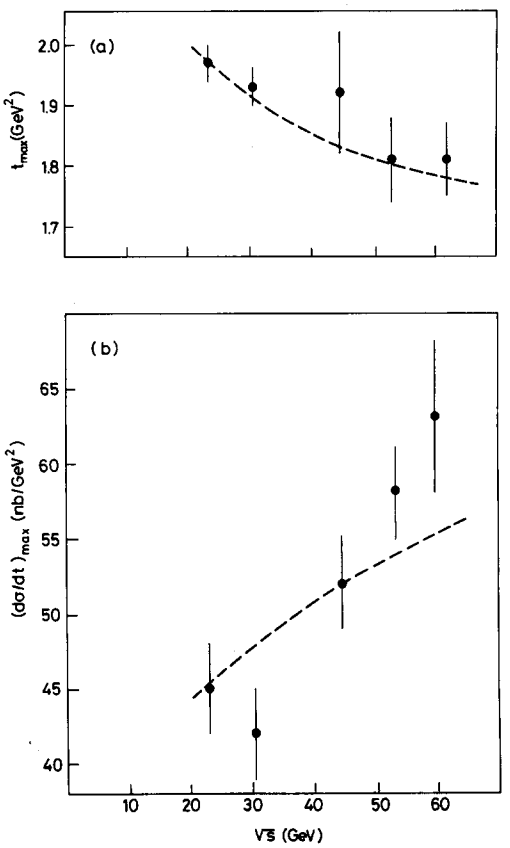

Fig. 17. (a) Position and (b) differential cross section of the second maximum as a function of $\sqrt{s}$. The dashed curves represent the $\sqrt{s}$ dependence of (a) $(1/\sigma_T)$ and of (b) σ_T^2.

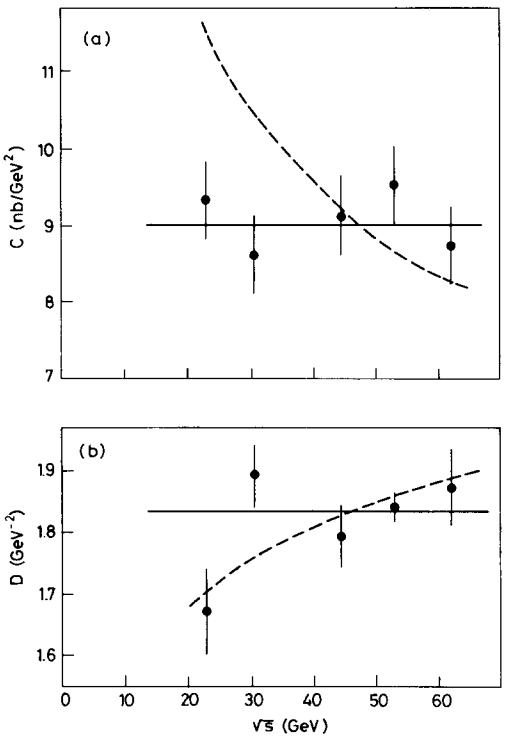

Fig. 18. Values of the parameters (a) C and (b) D of the exponential fit (eq. (4.4)) to the differential cross section between $|t| = 2.3$ and 5.1 GeV^2. The solid curves represent the parameters for a common fit to all five energies. The dashed curves show the predictions of geometrical scaling, normalized at $\sqrt{s} = 45$ GeV.

Table 5
Parameters of an exponential in $(|t| - 3\ \text{GeV}^2)$ (eq. (4.4)) as determined by a fit to the data in the t interval from 2.3 to 5.1 GeV^2: numbers in brackets give the degrees of freedom

$\sqrt{s}$ (GeV)	χ^2	C [a] (nb/GeV^2)	D [b] (GeV^{-2})
23.4	22.8 (23)	9.3 ± 0.5	1.67 ± 0.07
30.5	20.8 (23)	8.6 ± 0.5	1.89 ± 0.05
44.6	20.6 (23)	9.1 ± 0.5	1.79 ± 0.05
52.8	14.4 (23)	9.5 ± 0.5	1.84 ± 0.02
62.1	12.3 (23)	8.7 ± 0.5	1.87 ± 0.06
all	102 (123)	9.0 ± 0.5	1.835 ± 0.010

[a] Value of $d\sigma/dt$ at $t = -3$ GeV^2.
[b] Slope parameter of the exponential.

mine slope values. At this energy, the last three events observed are in the t bin 9.5 to 10 GeV^2. However, as shown in fig. 8, the acceptance of the apparatus extends much further, and we display upper limits on $d\sigma/dt$ which we derive from the zero-event information in fig. 19. The upper limits for $\Delta\sigma/\Delta t$ between 10 and 18 GeV^2 are evaluated for 90% confidence (<2.3 events observed) and depend on the bin width Δt. Although it may not be very useful to extract a slope from upper limits, we would like to quote the result of two maximum-likelihood fits: assuming a constant exponential slope D' in the t interval between 6.0 and 10.0 GeV^2, we find $D' = (0.88 \pm 0.13)$ GeV^{-2}; and with the same assumption in the t interval between 6.0 and 20 GeV^2, $D' = (1.00 \pm 0.12)$ GeV^{-2}. Both fits are good. These slope values are significantly smaller than in the interval from 2.3 to 5.1 GeV^2; we therefore conclude that there is a definite change of slope beyond $|t| = 5$ GeV^2.

This change of slope is not necessarily a break; an alternative description of the large-t data by an exponential in $p_T \approx \sqrt{-t}$, has been proposed by many authors [30–32]. We have tried to find which is the largest t range allowing a good fit at all five energies to the following expression:

$$d\sigma/dt = \tilde{C} \exp[-\tilde{D}(\sqrt{-t} - 1.8\ \text{GeV})] \ , \tag{4.5}$$

and find good agreement for $|t| > 2.7$ GeV^2, extending to 10 GeV^2 for $\sqrt{s} = 53$

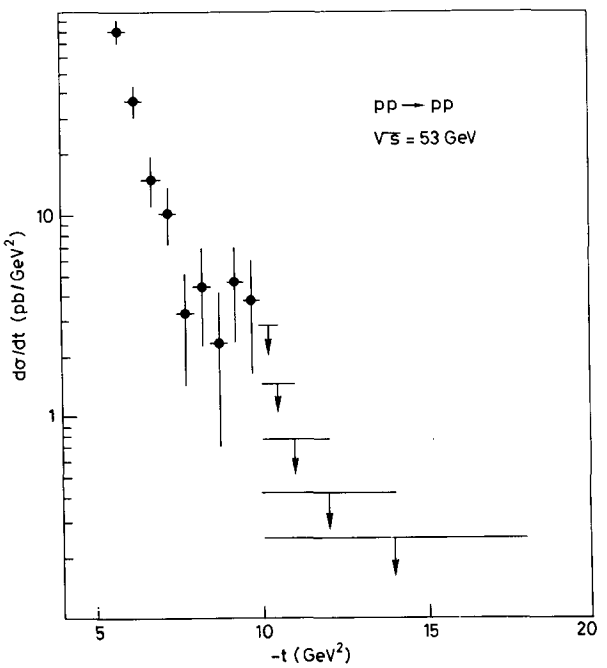

Fig. 19. Differential cross sections and upper limits (90% confidence) for the large-t region at $\sqrt{s} = 53$ GeV.

GeV. A common fit of all five cross-section data sets in this t region gives $C = (5.65 \pm 0.29)\text{nb/GeV}^2$ and $\tilde{D} = (7.07 \pm 0.05)\text{GeV}^{-1}$, with $\chi^2 = 110.8$ for 129 d.f. Fig. 20 shows the differential cross sections at 53 GeV as a function of p_T together with the best fit.

4.6. *The phase of the scattering amplitude*

It has been shown by several authors [33] that there is a simple and rather model-independent way of extracting the phase of the scattering amplitude from the s-de-

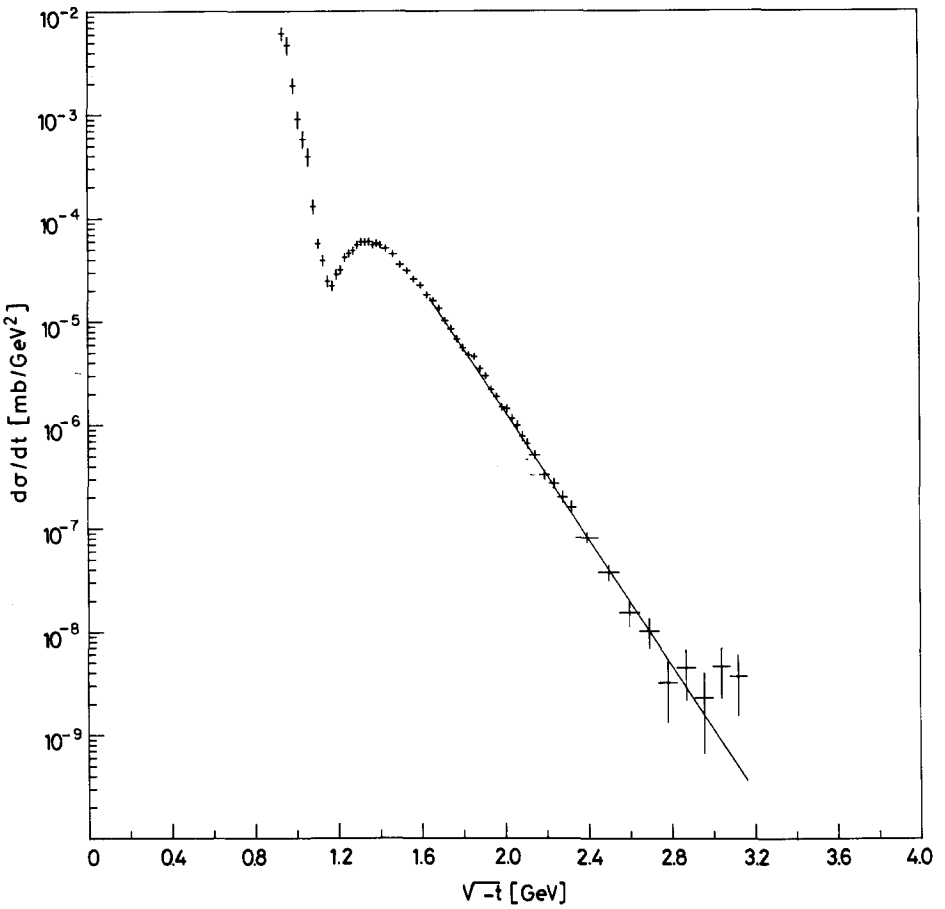

Fig. 20. Differential cross section as a function of $p_T = \sqrt{-t}$ for $\sqrt{s} = 53$ GeV. The curve represents the best fit to an exponential for $|t| \geq 2.7$ GeV^2.

pendence of the differential cross section. As long as real parts do not dominate *, $|\mathrm{Re}\, f/\mathrm{Im}\, f| < 1$, and the amplitude has even crossing symmetry, the result is well-approximated by [34]

$$\frac{\mathrm{Re}\, f}{\mathrm{Im}\, f} = \tan\left(\tfrac{1}{4}\pi \frac{\mathrm{d}}{\mathrm{d}\ln s} \ln\frac{\mathrm{d}\sigma}{\mathrm{d}t}\right) . \tag{4.6}$$

We have assumed even crossing symmetry for all t values and have applied this derivative analyticity relation to our data. The validity of this assumption is supported by the well-known fact that all measured amplitudes with odd crossing symmetry are strongly energy dependent; hence there is no need for a pomeron-like exchange amplitude with odd crossing symmetry in any known hadronic reaction [35].

Fig. 21 shows $\ln(\mathrm{d}\sigma/\mathrm{d}t)$ as a function of $\ln s$ for various values of t. The points shown are not raw data but values smoothened in t using eqs. (4.1) and (4.2) and appropriate error propagation. For $|t| \leqslant 1.2$ GeV^2 and for $|t| > 1.6$ GeV^2 it is possible to fit a straight line to the data points; the data are compatible with an s-independent ratio of $\mathrm{Re}\, f/\mathrm{Im}\, f$. By approaching $|t| = 1.2$ GeV^2 from below, the real-part contribution increases, and for $|t| > 1.6$ GeV^2 it decreases again. In between there appears to be a pole of the ratio $\mathrm{Re}\, f/\mathrm{Im}\, f$, because of a crossing through zero of the imaginary part, in agreement with eq. (4.2). Eq. (4.6) cannot be used to determine precise values of $\mathrm{Re}\, f/\mathrm{Im}\, f$ near this pole; such a determination would require the use of integral dispersion relations [36]. The actual t position of the pole depends on s as does the minimum position t_{min} of the cross section. This is well seen in fig. 21 for $t = -1.4$ GeV^2, where the slope $(\mathrm{d}/\mathrm{d}\ln s)\ln(\mathrm{d}\sigma/\mathrm{d}t)$ between 23 and 31 GeV is negative, whereas between 45 and 62 GeV it is already positive.

Fig. 22 shows the ratio $\mathrm{Re}\, f/\mathrm{Im}\, f$ as determined from the fitted slopes of the straight lines drawn in fig. 21. The full points correspond to a fit over the full ISR energy range, whereas the open points correspond to the narrower energy range from $\sqrt{s} = 45$ to 62 GeV. For $|t| \geqslant 2.2$ GeV^2, $\mathrm{Re}\, f/\mathrm{Im}\, f$ is compatible with zero in agreement with the observed energy independence of the parameters C and D as described in subsect. 4.5. For $|t| \geqslant 5$ GeV^2, no conclusion is possible owing to lack of data at more than one energy.

4.7. Comparison with other experiments

At present there exist only results of two experiments on elastic proton-proton scattering which partially overlap with ours in s and t; one was performed at the ISR and the other one at FNAL. The ISR experiment of Böhm et al., [2] has determined unnormalized differential cross sections between $\sqrt{s} = 23$ and 53 GeV. The statistics and hence the t range covered are much smaller than for the present experiment owing to lower ISR luminosities in 1972. Cross sections cannot be compared, but the shapes of $\mathrm{d}\sigma/\mathrm{d}t$ agree well in the t ranges where the two experiments overlap.

* Spin effects have been neglected.

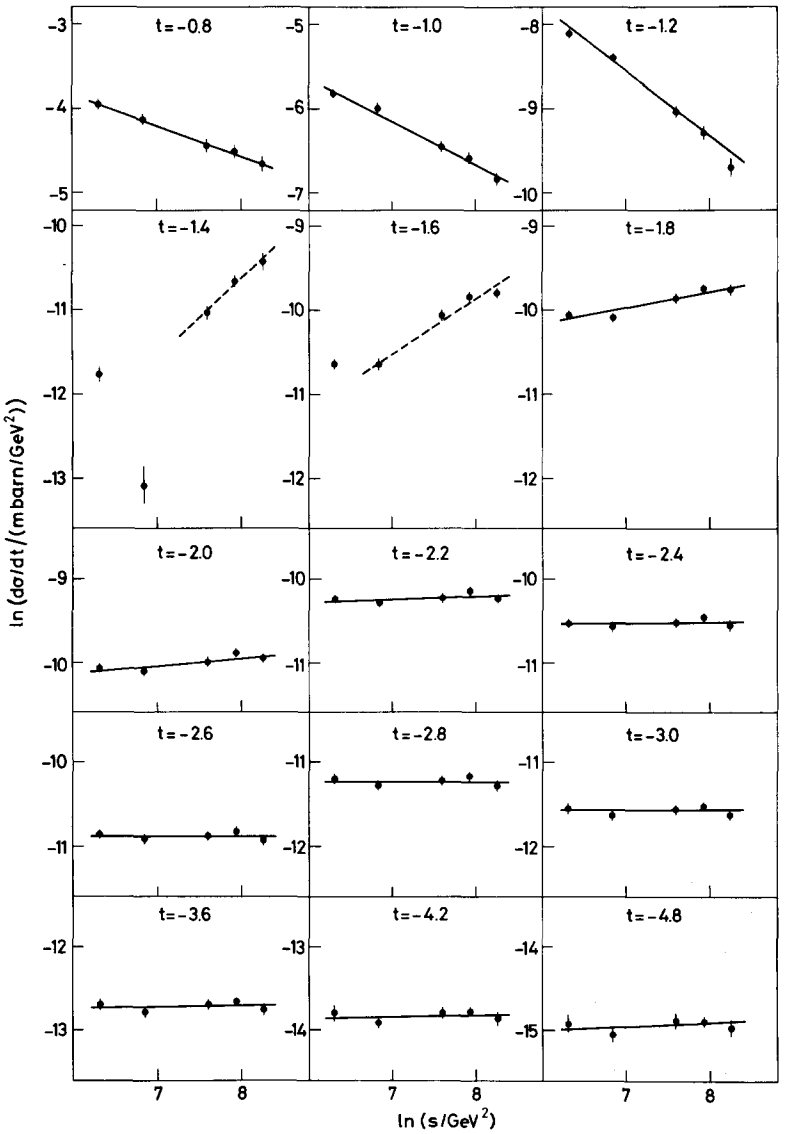

Fig. 21. Differential cross section as a function of s on a double-logarithmic scale for t values of 0.8 to 4.8 GeV^2. The curves are best fit straight lines; their slopes are proportional to Re f/Im f.

The experiment of Hartmann et al. [37] * at FNAL has determined normalized differential cross sections at p_{lab} = 200 and 400 GeV for $-t$ = 5 to 12 GeV^2. The differential cross sections at 200 GeV are found to be higher than ours at $\sqrt{s}$ = 53

* This letter covers only the data at 200 GeV. Preliminary 400 GeV data are shown in ref. [38].

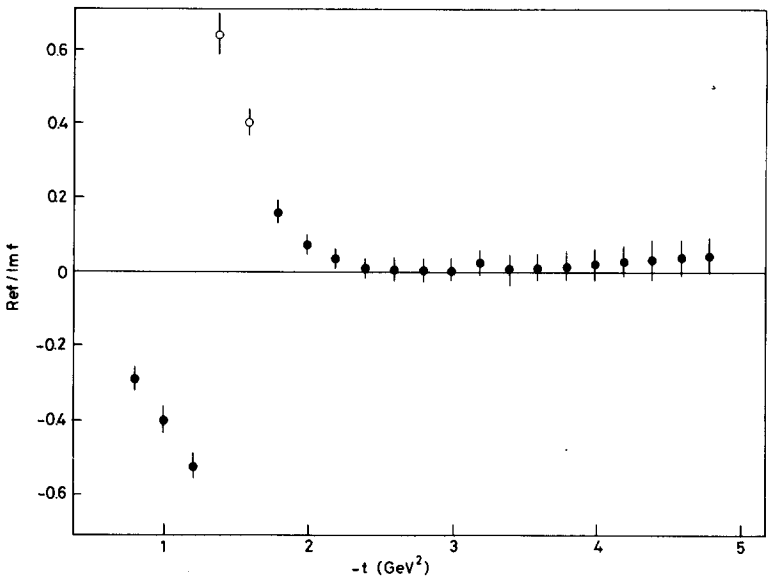

Fig. 22. Re f/Im f as a function of t, determined from fig. 21. Full points correspond to the full ISR energy range, open points to the limited range 45 to 62 GeV. Note the pole-like behaviour at the minimum.

GeV, but preliminary results at 400 GeV are at the same level as ours. Fig. 23 summarizes the energy dependence for fixed t values [38] of 5.0 and 6.0 GeV^2 including lower energy results [39]. There is a strong decrease with energy, suddenly levelling off at the lower end of the ISR energy range. At lower $|t|$ values, this levelling off takes place already at lower s values.

This s dependence may be interpreted as for $t = 0$. The elastic amplitude is built up by strong real parts due to exchange forces which are rapidly decreasing with energy, and by almost purely imaginary amplitudes due to diffraction which have nearly no energy dependence. At $t = -6$ GeV^2, the exchange contributions have vanished at $p_{\mathrm{lab}} \approx 400$ GeV, and diffraction alone survives.

5. Discussion

Assuming that a nearly energy-independent elastic amplitude is dominantly even crossing symmetric and therefore allows the application of a derivative analyticity relation as given by eq. (4.6), we conclude that the differential cross sections are dominated by an imaginary amplitude due to diffraction. We therefore limit our discussion to diffraction models.

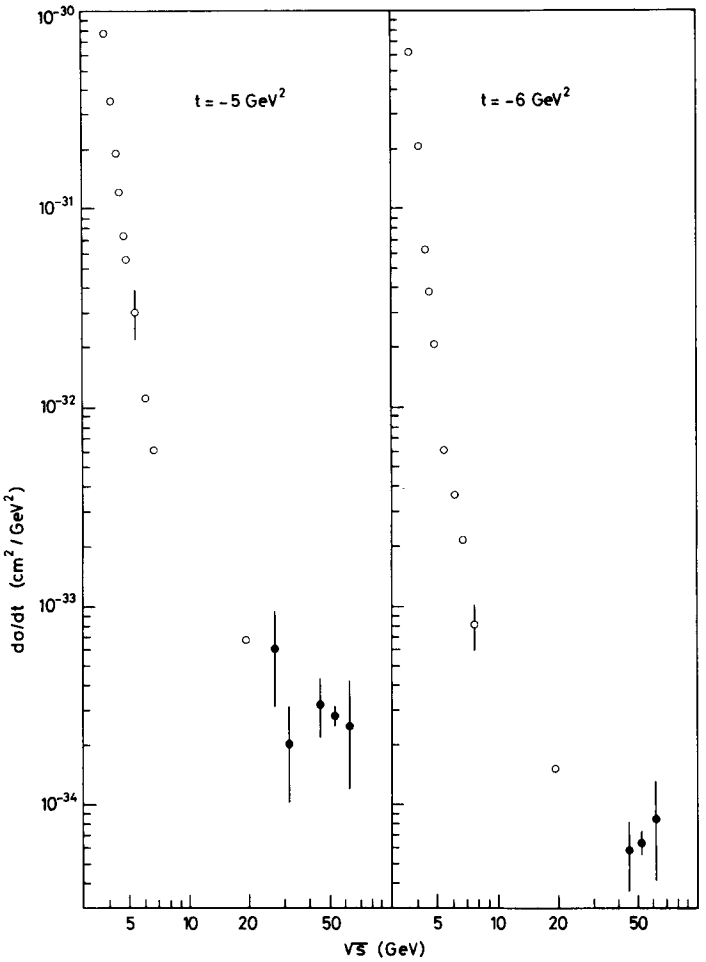

Fig. 23. Energy dependence of the differential cross section at t values of 5 GeV^2 and 6 GeV^2. Note the flattening out at ISR energies. Low-energy data are from ref. [39].

5.1. *The s-channel models*

The s-channel models attempt to describe diffraction by absorptive regions in the two-dimensional impact parameter space. Absorption can be represented as a function of the impact parameter b and of the energy variable s, and the most appropriate function is the eikonal $\Omega(b, s)$. In the model of Chou and Yang [40], the eikonal is proportional to the convolution of the charge density of the colliding hadrons. The Fourier transformation of the eikonal is hence proportional to the square of the electromagnetic form factor. The main predictions of this model are: (a) that

the differential cross sections approach an energy-independent limit, and (b) that several diffraction minima and maxima should occur. Both predictions are incompatible with our data. The observed energy dependence of the minimum position contradicts (a), and the absence of a second minimum up to $|t| = 10$ GeV^2 contradicts (b).

Constituent models [41] specify the eikonal according to Glauber's hypothesis [42]. The constituents, e.g., valence quarks, scatter elastically on each other, and the eikonal observed is the sum of all quark-quark eikonals. These models have more freedom in parametrizing the scattering amplitude than the Chou-Yang model, e.g., by choosing the number of constituents, the form of the quark-quark eikonal, and the quark distribution inside the proton. Nevertheless, Glauber's mechanism imposes specific features such as (a) the appearance of further diffraction minima, and (b) the ratio of the slope values between the different minima. None of the models known to us can describe the observed differential cross section without changing the relative strength of the successive terms in the multiple scattering expansion, thus artificially destroying Glauber's predictions.

The failure of the Glauber model may be interpreted in different ways. One way is to assume that Glauber's mechanism is not adequate, e.g., one should take into account the inelastic quark-quark scattering as well. This is equivalent to replacing the overall scalar eikonal $\Omega(s, b)$ by a matrix eikonal $\Omega_{ij}(s, b)$ containing the elastic channel ($i = 1$) as well as all diffractive inelastic channels ($i = 2, 3, ..., N$). The first term in the eikonal series is still Ω_{11}, but the second term Ω_{11}^2 is replaced by $\Omega_{11}^2 + \Omega_{12}\Omega_{21} + ... + \Omega_{1N}\Omega_{N1}$, including all transitions from the incident channel to an inelastic channel in a first interaction followed by the transition from this inelastic channel back to the elastic channel in the second interaction. A model with $N = 3$ and simple expressions for $\Omega_{ij}(s, b)$ has been presented by Crozier and Webber [43], which gives a good description of all features of the data presented here.

Another way is to assume that the elastic scattering amplitude in these s and t ranges is not due to a fixed number of valence quarks but to other objects, e.g., to gluons [44]. Analysing our data in the framework of a gluon model, Van Hove [45] arrives at two conclusions: (a) the gluon-gluon scattering amplitude is completely black, not only at zero impact parameter but also in a finite region around; (b) the gluon density is concentrated around the centre of the proton.

A model recently developed by Schrempp and Schrempp [32] attempts at describing high-energy hadron scattering by diffraction in three dimensions. The two transverse dimensions of the absorption region determine σ_{tot} and small-t elastic scattering, the longitudinal dimension determines the elastic cross section in the t range beyond 2 GeV^2. If the absorption region is a long prolate spheroid ("fire sausage"), as suggested by an interpretation of particle production on nuclei [46], the elastic cross section in this t region should be proportional to an exponential in transverse momentum p_T, $\exp(-bp_T)$, and there should be no second minimum. Both predictions agree with the data. The observed energy independence of b implies that the length of the absorption spheroid increases proportionally to $\sqrt{s}$.

5.2. The t-channel models

5.2.1. Regge poles. The simplest t-channel model, describing elastic scattering by the exchange of a single Regge pole,

$$\frac{d\sigma}{dt} = |g(t)\, e^{-i\pi\alpha(t)/2} s^{\alpha(t)-1}|^2 , \tag{5.1}$$

is certainly ruled out by our data, since we observe that the position of the diffraction minimum is energy dependent, whereas the residue function $g(t)$, which alone could give rise to a minimum, should not depend on the energy.

We have tried to describe our data in the t interval from 0.9 to 5.1 GeV^2 by the superposition of two Regge poles with exponential residue functions:

$$\frac{d\sigma}{dt} = |\sqrt{A}\, e^{Bt/2}\, e^{-i\pi\alpha_1(t)/2} s^{\alpha_1(t)-1} - \sqrt{C}\, e^{Dt/2}\, e^{-i\pi\alpha_2(t)/2}\, s^{\alpha_2(t)-1}|^2 . \tag{5.2}$$

Assuming linear Regge trajectories, the fit fails (χ^2 = 544 for 244 d.f.), mainly because the model has a weaker energy dependence at the diffraction minimum than that of the data.

The superposition of three Regge poles, where two of them are pomeron-like and one of them has a small intercept $\alpha_3(0) \approx 0$, has been proposed by Phillips and Barger [28]. Using eight free parameters, we obtain a good fit (χ^2 = 227 for 241 d.f.) to the data in the t interval between 0.9 and 5 GeV^2. This description is, however, not very attractive since the asymptotic description of the small-t region requires the presence of Regge cuts anyhow.

5.2.2. Regge cuts. A simple model with a pomeron pole and a two-pomeron cut (P ⊗ P) has been adapted by Collins and Gault [47] to describe our data at $\sqrt{s}$ = 53 GeV. The agreement with the data is excellent. However, the best fit parameters are theoretically not satisfactory as they violate the Froissart bound [48] at higher energies. This difficulty may be solved by including multiple-pomeron iterations, but in the parametrization of this model already the addition of a three-pomeron term (P ⊗ P ⊗ P) leads to disagreement with the data.

Adding up all possible multiple-pomeron contributions is a complicated algorithm which has been solved in the reggeon field theory [49]. Above a certain transition energy, the value of which is uncertain at present, the multi-pomeron sum converges towards a simple scaling function, often called the fully renormalized pomeron. Deviations from this asymptotic pomeron sum fall roughly like $1/\ln s$, but their absolute values are unknown and therefore do not allow us to make a quantitative comparison with the data. We may, however, naively assume that the deviation is already small at ISR energies and identify the fully renormalized pomeron with the

observed geometrical scaling property of the elastic cross section which is discussed below.

5.3. Geometrical scaling

The concept of geometrical scaling (GS), as we shall use it in this subsection, has been first invoked in an attempt [5] to understand the observed scaling properties of particle production in the s-channel [50]. An earlier result, that rising total cross sections must lead to scaling elastic scattering cross sections, was obtained by Auberson et al. [4]. Including also scaling real parts of the scattering amplitude [51], one may interpret GS as a property of a Regge cut or of the fully renormalized pomeron of the reggeon calculus as discussed in subsect. 5.2.

Neglecting the real part of the scattering amplitude, GS predicts the following equality at any two (asymptotic) energies:

$$\frac{\mathrm{d}\sigma}{\mathrm{d}t}(s_1, t_1) = \frac{\sigma_{\mathrm{tot}}^2(s_1)}{\sigma_{\mathrm{tot}}^2(s_2)} \frac{\mathrm{d}\sigma}{\mathrm{d}t}\left[s_2, t_2 = \frac{\sigma_{\mathrm{tot}}(s_1)}{\sigma_{\mathrm{tot}}(s_2)} t_1\right]. \tag{5.3}$$

Fig. 24 shows the values of the expression on both sides of this equation for $\sqrt{s_1}$ = 23 GeV and $\sqrt{s_2}$ = 62 GeV, and fig. 25 for $\sqrt{s_1}$ = 45 GeV, $\sqrt{s_2}$ = 62 GeV. With the exception of the t region near the minimum where the real parts cannot be neglected, the scaling property is well-fulfilled in the second comparison, whereas it fails in the first one for t values beyond the diffraction minimum.

A scaling real part of the scattering amplitude may be introduced by replacing σ_{tot} in the following way:

$$i\sigma_{\mathrm{tot}} \to \sigma_{\mathrm{tot}}(i + \rho), \tag{5.4}$$

where $\rho = \mathrm{Re}\, f/\mathrm{Im}\, f$ at $t = 0$. This replacement leads to a relation between the cross sections at the diffraction minimum where $\mathrm{Im}\, f = 0$:

$$\frac{\mathrm{d}\sigma}{\mathrm{d}t}(s_1, t_{\mathrm{min}_1}) \approx \frac{\rho_1^2 \sigma_{\mathrm{tot}}^2(s_1)}{\rho_2^2 \sigma_{\mathrm{tot}}^2(s_2)} \frac{\mathrm{d}\sigma}{\mathrm{d}t}(s_2, t_{\mathrm{min}_2}), \tag{5.5}$$

for any pair of asymptotic values s_1 and s_2. This relation has been obtained before in a different way by Grein and Kroll [51].

The GS predictions expressed in eqs. (5.3) and (5.5) for the energy dependence of t_0, t_{min}, $(\mathrm{d}\sigma/\mathrm{d}t)\, t_{\mathrm{max}}$, C, and D are shown as dashed curves in figs. 15 to 18. Values for σ_{tot} and ρ are taken from the most recent experiments at the ISR [52,19] and at FNAL [29]. None of the quantities shows perfect agreement over the full ISR range, but all of them agree well with GS in the restricted energy range from 45 to 62 GeV.

We have also tested GS by an overall χ^2 fit to the cross sections at all five energies and to the upper three energies alone. We have tried three different forms in their

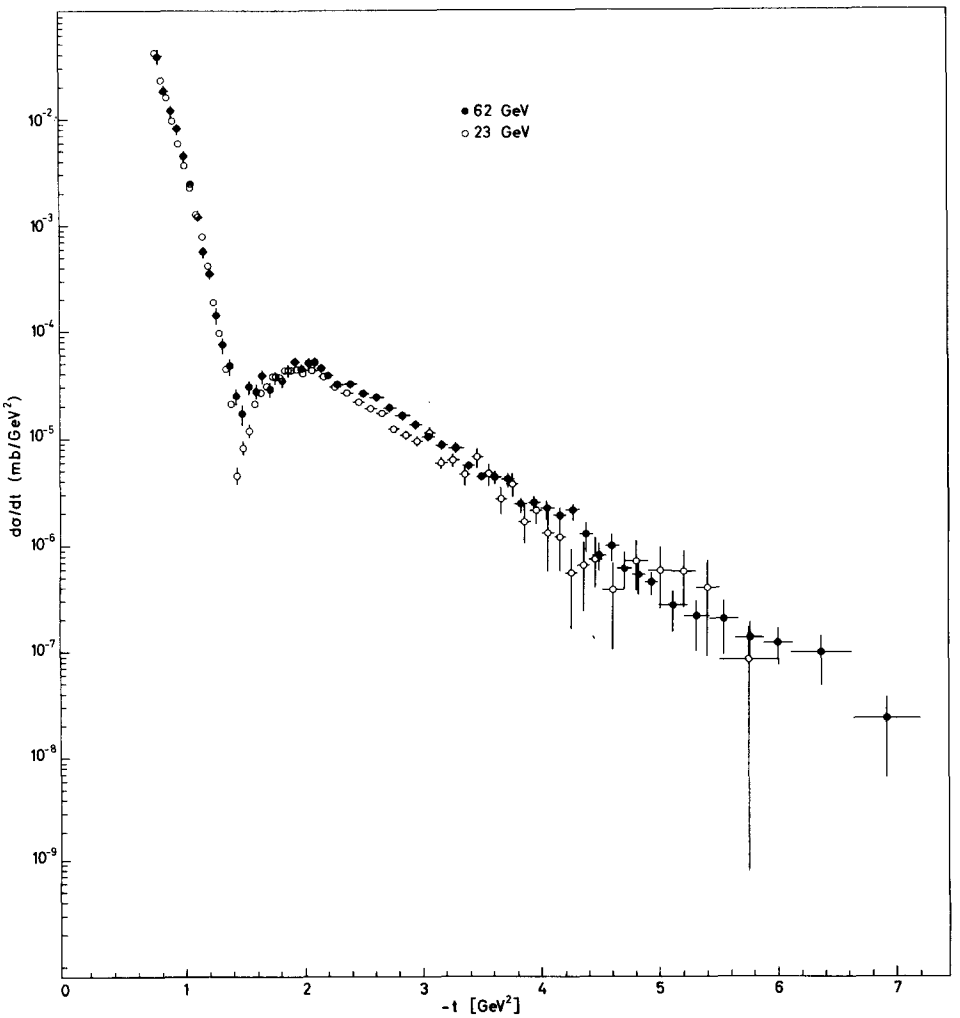

Fig. 24. Comparison of the t dependence of the differential cross sections at $\sqrt{s}$ = 23 GeV and 62 GeV. Cross sections and t values of the higher energy have been scaled according to geometrical scaling (eq. (5.3)).

appropriate t regions:

$$\frac{d\sigma}{dt} = A\sigma_{tot}^2(1+\rho^2)\, e^{B\sigma_{tot}t}, \qquad |t| \approx 2.3\text{–}5.1\ \text{GeV}^2\ , \tag{5.6}$$

$$\frac{d\sigma}{dt} = A\sigma_{tot}^2(1+\rho^2)\, e^{-B\sqrt{-\sigma_{tot}t}}, \qquad |t| \gtrsim 2.7\ \text{GeV}^2\ , \tag{5.7}$$

$$\frac{d\sigma}{dt} = |\sigma_{tot}(i+\rho)[\sqrt{A}\, e^{B\sigma_{tot}(1-i\rho)t/2} - \sqrt{C}\, e^{D\sigma_{tot}(1-i\rho)t/2}]|^2 , \quad |t| \approx 0.9\text{–}5.1 \text{ GeV}^2 . \tag{5.8}$$

The χ^2 values obtained for the fit are given in table 6; the goodness of the fits confirms that geometrical scaling is a reasonable approximation over the full ISR range and that it may be perfectly valid for $\sqrt{s} \geqslant 45$ GeV.

The data can also be described by the superposition of a Regge cut and a fixed Regge pole with $\alpha(t) = \alpha_0 + \alpha' t$,

$$\frac{d\sigma}{dt} = |\sqrt{A}\, \sigma_{tot}(i+\rho)\, e^{B\sigma_{tot}(1-i\rho)t/2} - \sqrt{C}\, e^{Dt/2}\, e^{-i\pi\alpha(t)/2}\, s^{\alpha(t)-1}|^2 , \tag{5.9}$$

where A, B, C, D, α_0, and α' are energy-independent constants.

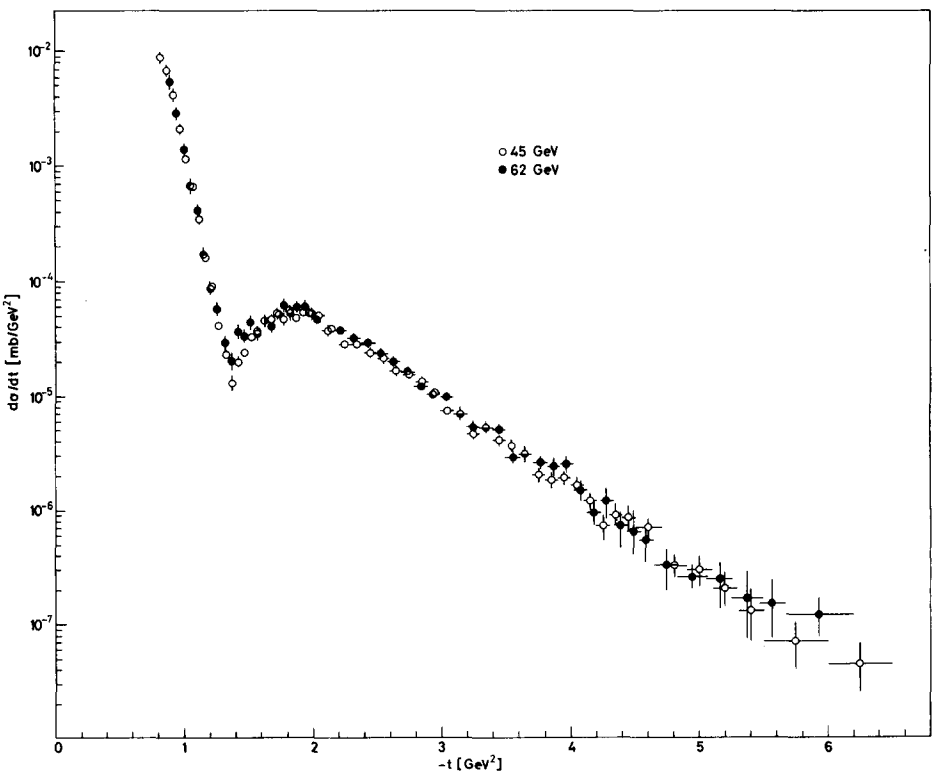

Fig. 25. Comparison of differential cross sections at $\sqrt{s}$ = 45 GeV and 62 GeV. Cross sections and t values of the higher energy have been scaled according to geometrical scaling (eq. (5.3)).

Table 6
Goodness-of-fit values for eqs. (5.6) to (5.8) to test geometrical scaling: numbers in brackets give the number of degrees of freedom

$\sqrt{s}$ (GeV)	χ^2 (eq. (5.6)) $\lvert t\rvert$ from 2.3 to 5.1 GeV^2	χ^2 (eq. (5.7)) $\lvert t\rvert \geq 2.7$ GeV^2	χ^2 (eq. (5.8)) $\lvert t\rvert$ from 0.9 to 5.1 GeV^2
23–62	160 (122)	157 (127)	320 (246)
45–62	48 (77)	62 (88)	133 (146)

We have tried three fits to the data over the full energy range from $\sqrt{s}$ = 23 to 62 GeV, and in the t interval from 0.9 to 5.1 GeV^2, using eq. (5.9) and varying the number of free parameters from six to four. The resulting parameters and χ^2 values are given in table 7. It should be noted that the overall χ^2 is good and that the

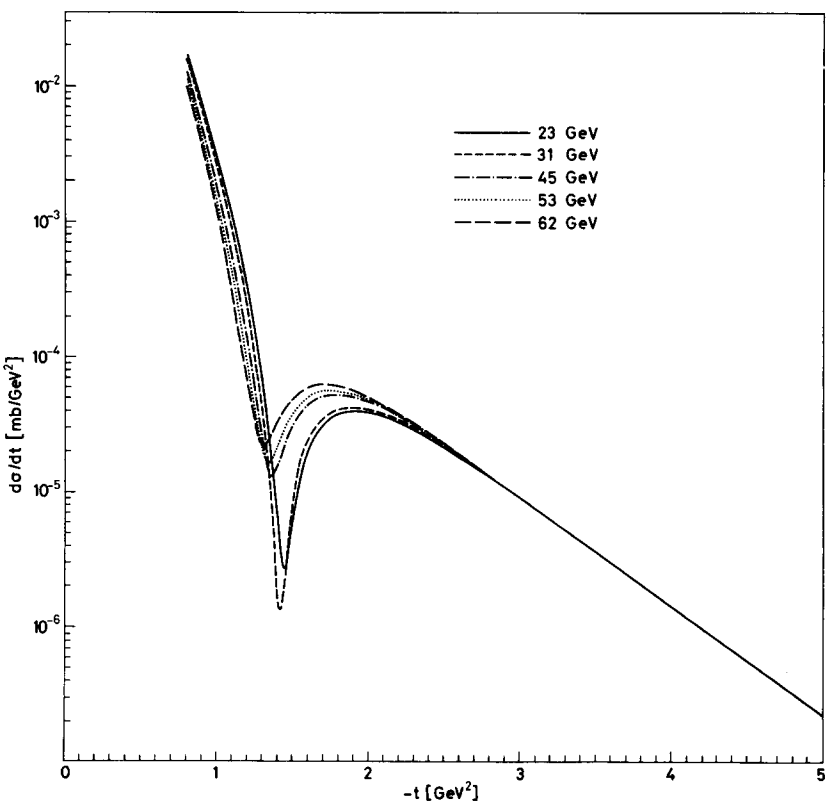

Fig. 26. Differential cross sections at five ISR energies according to the parameters determined by the best fit to a superposition of a Regge cut with the properties of geometrical scaling and a fixed Regge pole (eq. (5.9)). Values of parameters are given in table 7, fit C.

Table 7
Parameters of a superposition of a Regge cut (GS) and a fixed Regge pole as determined by a fit of eq. (5.9) to the data in the t interval from 0.9 to 5.1 GeV^2

Parameters	Fit A (6 parameters)	Fit B (5 parameters)	Fit C (4 parameters)
A (mb/GeV^2)	10.45 ± 0.07	11.47 ± 0.10	11.29 ± 0.07
B (GeV^{-2})	7.58 ± 0.01	7.68 ± 0.01	7.67 ± 0.07
C (mb/GeV^2)	0.0079 ± 0.0001	0.0032 ± 0.0002	0.0025 ± 0.0001
D (GeV^{-2})	2.31 ± 0.01	1.86 ± 0.02	1.858 ± 0.013
α_0	0.93 ± 0.07	0.98 ± 0.02	1.0
α'	−0.029 ± 0.010	0.0	0.0
ρ (23 GeV)	−0.021 ± 0.003	−0.028 ± 0.004	−0.035 ± 0.005
χ^2 (d.f.)	224 (244)	233 (245)	237 (246)

agreement is excellent in every s and t bin. The value of $\rho(\sqrt{s} = 23$ GeV) was assumed unknown and therefore determined by the fit (see table 7); it agrees well with recent measurements [29]. Fig. 26 shows the cross sections as calculated using eq. (5.9) with the best-fit values of four parameters and with $\alpha_0 = 1$ and $\alpha' = 0$ imposed.

6. Conclusions

We have measured differential cross sections of elastic pp scattering in the ISR energy range between $\sqrt{s} = 23$ and 62 GeV. At lower energies, this reaction has been successfully described by two mechanisms, diffraction and reggeon exchange. The diffractive mechanism is dominating at low values of t, and it is therefore customary to call the t interval between 0 and 0.2 GeV^2 the diffractive region. At larger t values, the differential cross sections are strongly energy dependent, thus indicating their non-diffractive origin. In this experiment, we find differential cross sections which are essentially independent of energy up to t values of 5 GeV^2, and we conclude that the diffractive region extends up to at least 5 GeV^2 in this energy range.

The forward peak of the differential cross section shows a weak energy dependence which can be attributed to the increasing size of the interaction range. The rising total cross section of pp collisions defines the scale for this s dependence. A consistent description of the elastic forward peak, by geometrical scaling [5,51], has been obtained for a large energy range from $\sqrt{s} = 6$ to 62 GeV by using the total cross section as a scale and a scaling real part of the scattering amplitude.

The forward peak is followed by a t region around the pronounced cross-section minimum at $t \approx -1.4$ GeV^2, which is showing stronger energy dependence. The position of the minimum changes with energy as $1/\sigma_{\text{tot}}$ as expected from the increasing size of the interaction range. The cross section at the minimum is pro-

portional to $\rho^2\sigma_{tot}^2$ for energies larger than $\sqrt{s}$ = 30 GeV, where ρ = Re f/Im f at t = 0. This result favours a description of the region near the minimum by a crossing through zero of the imaginary part of the scattering amplitude. The phase of the scattering amplitude is changing sign at the minimum.

A second component of diffraction scattering is observed in the t range from 2 to 5 GeV^2. Its t dependence is much weaker than for the forward peak and cannot be described by simple eikonal or constituent models connecting this region to the forward peak. However, a consistent description is possible [43] by an eikonal including inelastic diffractive channels in the context of the Good and Walker picture [53].

The energy dependence of the second diffraction component is compatible with geometrical scaling only at energies larger than or equal to $\sqrt{s}$ = 45 GeV. In the energy range 23 to 30 GeV we observe an additional weak energy dependence, at the diffraction minimum as well as between $|t|$ = 2 and 5 GeV^2, probably indicating contributions of exchange terms to the scattering amplitude. This scale-breaking behaviour is the same as for a bare pomeron pole, see eq. (5.9).

A new change of the slope of $d\sigma/dt$ is observed near $t = -6$ GeV^2, but no second diffraction minimum for t values up to 10 GeV^2, in contrast to the prediction of simple eikonal models of a recurrence of the first minimum.

We gratefully acknowledge the excellent help and the support of the ISR staff during the data-taking phase of this experiment. We are also most grateful to the SFM detector and data-handling group for their help, in particular to W. Bell, Ms. F. Blin, B. Heck, H. Grote, M. Metcalf, Ms. F. Ranjard and Z. Sekera. Essential technical contributions have been made by W. Wilmsen, B. Friend, A. King and X. Mehlführer. We wish to thank Profs. N. Kwak and E. Lohrmann for their contributions to earlier parts of the experiment. We would like to thank a large community of theoretical physicists for their interest in this work and for the numerous discussions we have had with them. We gratefully extend our thanks to the computer staffs in Hamburg, Heidelberg and Vienna for their help during the analysis work of the experiment, in particular to O. Hell (Hamburg) and Miss I. Spinnler (Heidelberg). The group from the University of Hamburg wishes to acknowledge financial support from the Bundesministerium für Forschung und Technologie, Germany. The Vienna group gratefully acknowledges support from the Fonds zur Förderung der wissenschaftlichen Forschung, Austria.

References

[1] M. Holder et al., Phys. Lett. 35B (1971) 355; 36B (1971) 400;
U. Amaldi et al., Phys. Lett. 36B (1971) 504; 43B (1974) 231;
G. Barbiellini et al., Phys. Lett. 39B (1972) 663.
[2] A. Böhm et al., Phys. Lett. 49B (1974) 491.
[3] U. Amaldi et al., Phys. Lett. 44B (1973) 112;
S.R. Amendiola et al., Phys. Lett. 44B (1973) 119.

[4] G. Auberson et al., Phys. Rev. D3 (1971) 3185.
[5] J. Dias de Deus, Nucl. Phys. B59 (1973) 213;
A.J. Buras and J. Dias de Deus, Nucl. Phys. B71 (1974) 481.
[6] H. de Kerret et al., Phys. Lett. 63B (1976) 477, 483.
[7a] N. Kwak et al., Phys. Lett. 62B (1976) 359.
[7b] H. de Kerret et al., Phys. Lett. 69B (1977) 372.
[8] H. de Kerret et al., Phys. Lett. 68B (1977) 385.
[9] E. Nagy et al., Contribution to 17th Int. Conf. on High-energy physics, London, 1974.
[10] N. Kwak et al., Phys. Lett. 58B (1975) 233.
[11] H. de Kerret et al., Phys. Lett. 62B (1976) 363.
[12] H. de Kerret et al., Phys. Lett. 68B (1977) 374.
[13] K. Johnson, Proc. Int. Conf. on Elementary particles, Amsterdam, 1971, ed. A. Tenner and M. Veltman (North-Holland, Amsterdam, 1972) p. 373.
[14] R. Bouclier et al., Nucl. Instr. 115 (1974) 235.
[15] R. Bouclier et al., Nucl. Instr. 125 (1975) 19.
[16] W. Bell et al., Nucl. Instr. 124 (1975) 437.
[17] A. Brandt et al., Nucl. Instr. 126 (1975) 513.
[18] S. Van der Meer, CERN Internal Report ISR-PO/68-31 (1968).
[19] U. Amaldi et al., Phys. Lett. 66B (1977) 390.
[20] A. Fröhlich, H. Grote, C. Onions and F. Ranjard, CERN Internal Report DD/76-5 (1976).
[21] M. Metcalf et al., CERN 73-2 (1973).
[22] J.J. Aubert and C. Broll, Nucl. Instr. 120 (1974) 137.
[23] J. Munkres, J. Soc. Indust. Appl. Math. 5 (1957) 1.
[24] C. Berge, Graphs and hypergraphs (North-Holland, Amsterdam, 1973).
[25] M. Regler, Acta Phys. Austriaca 49 (1978) 1.
[26] A. Brandt, Thesis, Universität Hamburg, 1975.
[27] Fermilab Single-Arm Spectrometer Group, Phys. Rev. Lett. 35 (1975) 1195.
[28] R.J.N. Phillips and V. Barger, Phys. Lett. 46B (1973) 412.
[29] E. Jenkins et al., The real part of the pp and pd forward scattering amplitudes from 50 to 400 GeV, Fermilab-PUB-78/35-EXP (April, 1978).
[30] J. Orear, Phys. Lett. 13 (1964) 190.
[31] M.M. Islam and J. Rosen, Phys. Rev. Lett. 22 (1969) 502.
[32] B. Schrempp and F. Schrempp, Phys. Lett. 70B (1977) 88.
[33] V.N. Gribov and A. Migdal, Yad. Fiz. 8 (1968) 1002;
J.B. Bronzan, Argonne Symposium on the pomeron, ANL/HEP-7327 (1973), p. 33;
J.B. Bronzan et al., Phys. Lett. 49B (1974) 272;
J. Fischer and P. Kolar, Phys. Lett. 64B (1976) 45.
[34] U. Sukhatme, Proc. 12th Rencontre de Moriond, Flaine, 1977 (Institut National de Physique Nucléaire et de Physique des Particules, Paris, 1977), vol. II, p. 57.
[35] P. Kroll, private communication.
[36] W. Grein et al., Nucl. Phys. B89 (1975) 93.
[37] J.L. Hartmann et al., Phys. Rev. Lett. 39 (1977) 975.
[38] K. Winter, Proc. European Conf. on Particle physics, Budapest, 1977, ed. L. Jenik and I. Montvay (Central Research Institute for Physics, Budapest, Hungary, 1978), vol. 1, p. 55.
[39] A.N. Diddens, Compilation of data on elastic scattering, *in* Landolt-Börnstein, Zahlenwerke und Funktionen, Neue Serie vol. I7 (1973);
K.R. Schubert, *ibid.*, vol. I9, to be published.
[40] T.T. Chou and C.N. Yang, Phys. Rev. 170 (1968) 1591.
[41] L. Durand and R. Lipes, Phys. Rev. Lett. 20 (1968) 637;
M. Kac, Nucl. Phys. B62 (1973) 402;

S. Wakaizumi and M. Tanimoto, Phys. Lett. 70B (1977) 55.
[42] R.J. Glauber, High-energy collision theory (New York, 1959).
[43] P.J. Crozier and B.R. Webber, Nucl. Phys. B115 (1976) 509.
[44] L. Van Hove and K. Fialkowski, Nucl. Phys. B107 (1976) 211.
[45] L. Van Hove, preprint TH-2278-CERN (1977).
[46] L. Caneschi, Proc. 12th Rencontre de Moriond, Faline, 1977 (Institut National de Physique Nucléaire et de Physique des Particules, Paris, 1977), vol. II, p. 65.
[47] P.D.B. Collins and F.D. Gault, Regge cuts and large-t pp scattering, University of Durham preprint (November, 1977).
[48] M. Froissart, Phys. Rev. 123 (1961) 1053.
[49] Z. Koba et al., Nucl. Phys. B40 (1972) 317.
[51] W. Grein and P. Kroll, Phys. Lett. 58B (1975) 79.
[52] CERN-Pisa-Rome-Stony Brook Collaboration, Phys. Lett. 62B (1976) 460.
[53] M.L. Good and W.D. Walker, Phys. Rev. 120 (1960) 1857.